Front. Earth Sci. 2024, 18(1): 44–67
https://doi.org/10.1007/s11707-022-1058-2

RESEARCH ARTICLE

Geological modeling of coalbed methane reservoirs in the tectonically deformed coal seam group in the Dahebian block, western Guizhou, China

Yong SHU[1,3], Shuxun SANG (✉)[2,3,4], Xiaozhi ZHOU[1,3]

1 Key Laboratory of Coalbed Methane Resources and Reservoir Formation Process (Ministry of Education), China University of Mining and Technology, Xuzhou 221116, China
2 Carbon Neutrality Institute, China University of Mining and Technology, Xuzhou 221008, China
3 School of Resources and Geosciences, China University of Mining and Technology, Xuzhou 221116, China
4 Jiangsu Key Laboratory of Coal-based Greenhouse Gas Control and Utilization, China University of Mining and Technology, Xuzhou 221008, China

Abstract The widely spread Carboniferous-Permian coal seam group in southern China has great potential for coalbed methane resources, but the extensively developed tectonically deformed coal seriously restricts its development. Taking the Dahebian block in western Guizhou as the study area, the geological model of coalbed methane reservoirs in the tectonically deformed coal seam group was established, and the spatial distribution pattern of model parameters was clarified by clustering algorithms and factor analysis. The facies model suggests that the main coal body structures in Nos. 1, 4, and 7 coal seams are cataclastic coal and granulated coal, whereas the No. 11 coal seam is dominated by granulated coal, which has larger thicknesses and spreads more continuously. The *in situ* permeability of primary undeformed coal, cataclastic coal, granulated coal, and mylonitized coal reservoirs are 0.333 mD, 0.931 mD, 0.146 mD, and 0.099 mD, respectively, according to the production performance analysis method. The property model constructed by facies-controlled modeling reveals that Nos. 1, 4, and 7 coal seams have a wider high-permeability area, but the gas content is lower; the high-permeability area in the No. 11 coal seam is more limited, but the gas content is higher. The results of the self-organizing map neural network and K-means clustering indicate that the geological model can be divided into 6 clusters, the model parameter characteristics of the 6 clusters are summarized by data analysis in combination with 6 factors extracted by factor analysis, and the application of data analysis results in multi-layer coalbed methane co-development is presented. This study provides ideas for the geological modeling in the tectonically deformed coal seam group and its data analysis.

Keywords geological modeling, tectonically deformed coal, coal seam group, clustering algorithm, Dahebian block, western Guizhou

Received October 6, 2022; accepted November 29, 2022

E-mail: shxsang@cumt.edu.cn

1 Introduction

With the increasingly severe global energy shortage, countries around the world are making great efforts to develop unconventional oil and gas according to their resource conditions, especially for clean energy — unconventional natural gas, such as shale gas development in the United States and coalbed methane (CBM) development in China and Australia (Salmachi and Haghighi, 2012; Salmachi et al., 2019, 2021; Dunlop et al., 2020; Jiang et al., 2022; Li et al., 2022a). The annual production of CBM in China has exceeded 100×10^8 m^3 since 2020, the ground production in 2020 was 57.67×10^8 m^3, and the production was mainly from the Qinshui Basin and the eastern margin of the Ordos Basin (Cao et al., 2020; Jiang et al., 2022; Li et al., 2022a). With the advancement of CBM development technology, the strategic target of CBM in China has been gradually expanded to southern China (Qin and Gao, 2012; Qin et al., 2018; Tao et al., 2019). The widely spread Carboniferous-Permian coal seam group in southern China has great potential for CBM resources (Li et al., 2015; Qin et al., 2018; Guo et al., 2020). The constraints on CBM development in southern China at the present include: 1) despite the large

number of coal seams, their thickness is generally thin, requiring multi-layer co-development approaches to improve single-well production (Qin et al., 2018; Yang et al., 2018; Guo et al., 2020); 2) most coal-accumulating basins in southern China (such as western Guizhou) have experienced intense tectonic activity (Qin et al., 2018; Cheng and Pan, 2020), resulting in severe damage to the coal body structure and extensively developed tectonically deformed coal (TDC, in this article, refers to granulated coal (GC) and mylonitized coal (MC) in the Chinese National Coal Body Structure Classification Standard GB/T 30050-2013) with high gas content, low permeability and weak mechanical stability, severely limiting the application of development approaches such as hydraulic fracturing and horizontal well development (Li et al., 2017a; Ahamed et al., 2019; Tao et al., 2019; Cheng and Pan, 2020; Dunlop et al., 2020; Sang et al., 2020; Song et al., 2021). As a result, it is critical to clarify the distribution characteristics of the TDC and the coal seam group for CBM development in southern China.

Geological modeling is one of the most effective methods for characterizing the spatial distribution and reservoir properties of oil-gas reservoirs. Based on geophysical and sample test data, the methods of using geostatistical deterministic or stochastic simulation to establish a geological model that can accurately depict the spatial distribution of oil-gas reservoirs are relatively well established (Zhou et al., 2012; Zhou and Guan, 2016; Urych et al., 2019). However, geological modeling of TDC reservoirs still faces challenges. Some coal reservoir properties, such as gas content, could be obtained directly or indirectly through core desorption tests or the Langmuir isothermal sorption equation (Li et al., 2017b, 2022b). However, because of the fractured and loose coal body structure, it is challenging to obtain intact TDC samples for permeability, which is the critical physical property in CBM development, while reconstituted samples using pulverized coal could not accurately represent reservoir permeability under *in situ* conditions (Dong et al., 2018; Sang et al., 2020; Cheng and Lei, 2021). Well-logging, numerical simulation, well-testing, and production performance analysis are currently the most common methods for determining the *in situ* permeability of coal reservoirs. The mathematical model of the well-logging method simplifies coal to a homogeneous medium, and therefore the error in the results is generally large (Sibbit and Faivre, 1985; Shi et al., 2020). The disadvantages of the numerical simulation method are the complex parameter coupling relationships and the time-consuming process (Karacan, 2013; Awotunde, 2017; Shi et al., 2018). The well-testing method could accurately determine permeability, but obtaining the pressure recovery curve requires water injection and well shut-in, which is not conducive to the continuity of CBM development (Hamdi, 2014; Salmachi et al., 2019; Shi et al., 2019). The production performance analysis method, which processes production data to estimate permeability according to the flowing material balance equation, is less costly and easy to implement, making it an ideal alternative to well-testing (Shi et al., 2018, 2019, 2020; Zhu et al., 2018).

Due to a large number of coal seams in the coal seam group, it is difficult to conduct plane analysis and evaluation after the geological model was established, and there is a lack of established evaluation criteria. Furthermore, the analysis results may be subjective or one-sided because the human-made evaluation criteria are based on development experience or regional characteristics. The self-organizing map (SOM) neural network is an unsupervised artificial neural network algorithm for data mining and visualization, suitable for clustering and analyzing of unlabeled data (Kohonen, 1982, 1995). The use of the SOM neural network combined with another clustering algorithm has shown excellent application in the data analysis of hydrology, environment, and geochemistry (Choi et al., 2014; Chen et al., 2017; Brentan et al., 2018; Santos et al., 2020). Compared to the human-made evaluation criteria, unsupervised machine learning algorithms can reveal the underlying distribution patterns of data and obtain the classification or evaluation patterns that could reflect the data structure.

In this study, taking the Dahebian block in western Guizhou as the study area, geological modeling of CBM reservoirs in the TDC seam group and data analysis were conducted to clarify the spatial distribution pattern of model parameters. First, the Petrel software was used to establish the structural model and the facies model of coal body structures. Then the reservoir permeability was determined according to the production performance analysis method, and the property models were established by the facies-controlled method. Finally, the model parameters were clustered using the clustering algorithms, and data analysis methods were used to clarify the distribution pattern of model parameters. This study provides ideas for determining the permeability of TDC reservoirs, geological modeling of CBM reservoirs in the TDC seam group and its data analysis, which are significant for guiding the CBM development in the TDC seam group.

2 Geological setting

Western Guizhou, known as the west of the Zunyi-Guiyang-Ziyun line in Guizhou Province, includes the Liupanshui mining area, Zhina mining area, and Qianbei mining area, and accounts for more than 90% of the total CBM resources in Guizhou Province (Qin and Gao, 2012; Xu et al., 2016). The Dahebian block belongs to the Liupanshui mining area and is located in the west wing of the Dahebian syncline. The coal seam group is found in the Upper Permian Longtan Formation, and it consists of

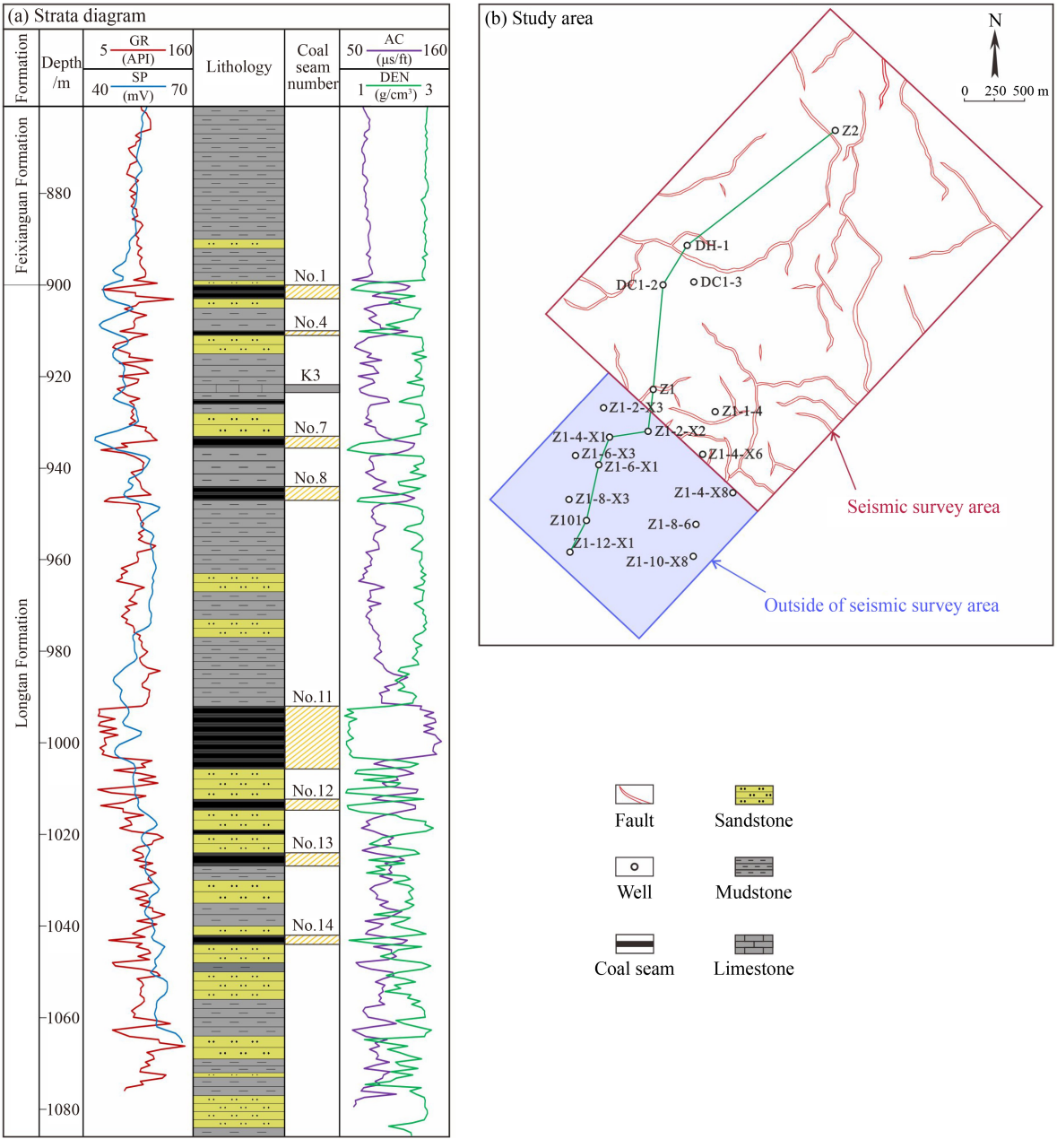

Fig. 1 Comprehensive geological map of the Dahebian block, western Guizhou.

a large number of coal seams that are generally thin (Fig. 1(a)). The areally-extended coal seams in the block include the Nos. 1, 4, 7, and 11 coal seams, with vitrinite reflectance ranging between 0.90% and 1.35%, indicating that the coal is of middle rank. The overlying Feixianguan Formation is dominated by siltstone and sandy mudstone, and the underlying Emeishan Basalt Formation is dominated by thick basalt, both of which are aquifers, impeding contact with the surface water and other aquifers, which is conducive to the preservation and development of CBM. A seismic survey has been carried out in the middle-north-east of the study area in preparation for the subsequent CBM development, and the CBM wells outside the seismic survey area in the south-west are more intensive (Fig. 1(b)). Therefore, the study area has abundant basic data on CBM exploration and development to perform geological modeling.

3 Materials and methods

3.1 Basic data

Drilling cores, well-logging data, seismic data, and CBM well production data serve as the foundation for this study. Seismic survey and data interpretation were done by the Bureau of Geophysical Prospecting INC, China National Petroleum Corporation. Coal body structure data

were first obtained from drill core logs of several wells, and the coal body structure in the remaining wells was predicted by training a support vector machine (SVM) coal body structure identification model with well-logging data as input data. The 5-fold cross-validation accuracy of the model is above 90%. The coal body structure thickness prediction in the seismic survey area is implemented by training an SVM coal body structure thickness prediction model with seismic attributes as input data. It is verified that the absolute error of thickness prediction for the thinner Nos. 1, 4, and 7 coal seams does not exceed 0.22 m, and the error for the thicker No. 11 coal seam is not greater than 0.67 m. All 4 types of coal body structures were identified in Nos. 1, 4, and 11 coal seams, and 3 types of coal body structures were found in the No. 7 coal seam except for the MC. In consideration of the focus and length of this article, the coal body structure data are regarded as known basic data, and the implementation would not be elaborated. The Petrel software from Schlumberger was used to construct a geological model of CBM reservoirs in the TDC seam group.

3.2 Production performance analysis method

The following conditions must be met by the production performance analysis method used in this study to determine permeability (Shi et al., 2018): 1) the gas reservoir should be undersaturated, implying a single-phase water flow stage; 2) the pressure drop does not propagate to the flow boundary; and 3) there should be no well interference during the single-phase water flow stage. The gas reservoir in the study area is undersaturated and has a short single-phase water flow stage, as shown in Figs. 6(a) and 6(b) in Section 4.3.1, which indicates a limited range of pressure drop in the single-phase water flow stage. The straight line section with a better fitting effect in the early stage of single-phase water flow is selected in the calculation process to meet the above conditions better.

For hydraulically fractured vertical wells, the reservoir pressure propagation distance perpendicular to the fracture expansion can be defined as (Shi et al., 2018)

$$R_{\mathrm{b}} = 0.72\sqrt{\frac{k_{\mathrm{f}}t}{\varphi\mu_{\mathrm{w}}C_{\mathrm{t}}}}, \tag{1}$$

where R_{b} is the reservoir pressure propagation distance perpendicular to the fracture expansion, m; k_{f} is the reservoir permeability, mD; t is the production time, d; φ is the reservoir porosity; μ_{w} is the water viscosity, mPa·s; C_{t} is the total compressibility of reservoirs, MPa^{-1}.

Since the pressure propagation of hydraulic fracturing vertical wells can be regarded as an ellipse with both ends of the fracture as the focus, the reservoir pressure propagation distance in the direction of the fracture can be expressed as (Shi et al., 2018):

$$R_{\mathrm{a}} = \sqrt{0.72^2\frac{k_{\mathrm{f}}t}{\varphi\mu_{\mathrm{w}}C_{\mathrm{t}}} + L_{\mathrm{f}}^2}, \tag{2}$$

where R_{a} is the reservoir pressure propagation distance in the direction of the fracture expansion, m; L_{f} is the half-length of the fracture, m.

The reservoir permeability is assumed constant during the single-phase water flow stage because the reservoir stress-sensitive effect is weak, and no gas desorption occurs to induce matrix shrinkage. According to Darcy's law, the water production per unit of time in a fractured straight well is given below (Lang, 2001; Shi et al., 2018):

$$Q_{\mathrm{w}}(t) = \frac{0.543k_{\mathrm{f}}h(p_{\mathrm{i}} - p_{\mathrm{wf}})}{\mu_{\mathrm{w}}B_{\mathrm{w}}\left(\ln\frac{R_a+R_b}{L_{\mathrm{f}}} + s\right)}, \tag{3}$$

where Q_{w} is the water production per unit time, m^3/d; h is the coal thickness, m; p_{i} is the initial reservoir pressure, MPa; p_{wf} is the bottom hole pressure, MPa; B_{w} is the water formation volume factor; and s is the skin factor.

A transformation of Eq. (3) yields

$$\int_0^t (p_{\mathrm{i}} - p_{\mathrm{wf}})\,\mathrm{d}t = \frac{\mu_{\mathrm{w}}B_{\mathrm{w}}}{0.543k_{\mathrm{f}}h}\int_0^t \ln\frac{R_a+R_b}{L_{\mathrm{f}}}Q_{\mathrm{w}}(t)\,\mathrm{d}t + \frac{\mu_{\mathrm{w}}B_{\mathrm{w}}s}{0.543k_{\mathrm{f}}h}\int_0^t Q_{\mathrm{w}}(t)\mathrm{d}t. \tag{4}$$

Both sides of Eq. (4) divided by the cumulative water production gives:

$$\frac{\int_0^t (p_{\mathrm{i}} - p_{\mathrm{wf}})\,\mathrm{d}t}{W_{\mathrm{p}}} = \frac{\mu_{\mathrm{w}}B_{\mathrm{w}}}{0.543k_{\mathrm{f}}h}\frac{\int_0^t \ln\frac{R_a+R_b}{L_{\mathrm{f}}}Q_{\mathrm{w}}(t)\,\mathrm{d}t}{W_{\mathrm{p}}} + \frac{\mu_{\mathrm{w}}B_{\mathrm{w}}s}{0.543k_{\mathrm{f}}h}, \tag{5}$$

where W_{p} is the cumulative water production, m^3.

Eq. (5) can be expressed by a linear equation:

$$Y = aX + b, \tag{6}$$

where

$$Y = \frac{\int_0^t (p_{\mathrm{i}} - p_{\mathrm{wf}})\,\mathrm{d}t}{W_{\mathrm{p}}}, \tag{7}$$

$$X = \frac{\int_0^t \ln\frac{R_a+R_b}{L_{\mathrm{f}}}Q_{\mathrm{w}}(t)\,\mathrm{d}t}{W_{\mathrm{p}}}, \tag{8}$$

$$a = \frac{\mu_{\mathrm{w}}B_{\mathrm{w}}}{0.543k_{\mathrm{f}}h}, \tag{9}$$

$$b = \frac{\mu_{\mathrm{w}}B_{\mathrm{w}}s}{0.543k_{\mathrm{f}}h}. \tag{10}$$

The permeability k_{f} and the skin factor s can be

determined by plotting points (X, Y) into a right-angle coordinate system and analyzing the slope a and intercept b of the fitted straight line. The specific process is as follows: (a) substitute the water production and reservoir pressure data into Eq. (7) to calculate Y; (b) assume a permeability k_{fa}, substitute k_{fa} and other parameters into Eq. (8) to calculate X and obtain a fitted straight line; (c) substitute the slope a of the straight line into Eq. (9) to obtain another permeability k_{fb}; (d) adjust k_{fa} and repeat steps (b) and (c) until the difference between k_{fa} and k_{fb} is less than the tolerance (10^{-3}), at which point we can assume that the exact permeability k_f is obtained, and the skin factor s can be obtained by substituting k_f and intercept b into Eq. (10). More detailed methods can be found in Shi et al. (2018, 2019, 2020).

The multiple development layers of CBM wells are simplified to a single layer, and the thickness is the total thickness of all layers. Assuming a stable distribution of permeability for all types of coal body structure reservoirs in the study area, the following relationship exists between the overall permeability and the thickness proportion of coal body structure:

$$k_f = k_{fUC}P_{UC} + k_{fCC}P_{CC} + k_{fGC}P_{GC} + k_{fMC}P_{MC}, \quad (11)$$

where k_{fUC}, k_{fCC}, k_{fGC}, and k_{fMC} are the permeability of primary undeformed coal (UC), cataclastic coal (CC), GC, and MC, respectively, mD; P_{UC}, P_{CC}, P_{GC}, and P_{MC} are the thickness proportions of UC, CC, GC, and MC, respectively.

Production data from 22 CBM wells were collected in this study. By substituting the permeability determined by the production performance analysis method and the proportion of coal body structure thickness into Eq. (11) to form a set of overdetermined equations. The approximate solution of the reservoir permeability of the 4 types of coal body structure could be obtained by using the least-squares method.

3.3 Calculation of coal gas content

CBM is primarily stored in coal reservoirs in the adsorbed state, and the adsorption volume can be described using the Langmuir isothermal adsorption equation (Langmuir, 1918; Li et al., 2013). The coal gas content is defined as

$$C_c = \frac{V_L P}{P_L + P} S_c, \quad (12)$$

where C_c is the coal gas content, m^3/t; V_L is the Langmuir volume, m^3/t; P_L is the Langmuir pressure, MPa; P is the reservoir pressure, MPa; S_c is the gas saturation.

3.4 Self-organizing map neural network

The term "self-organization" refers to the ability of SOM neural networks to learn and organize information similar to the human brain, adaptively adjusting the network through the regularity of input information (Kohonen, 1982; Mukherjee, 1997; Kalteh et al., 2008; Chen et al., 2017; Li et al., 2022c). The basic idea and goal of the SOM neural network are to nonlinearly convert high-dimensional input data into a low-dimensional network topology of neurons in an orderly fashion (Fig. 2). The SOM neural network consists of an input layer and an output layer (also known as the competitive layer). The input vector in the input layer is connected to each neuron in the output layer via the weight vectors, and the number of neurons is equal to the number of clusters. The neurons in the output layer are connected to adjacent neurons in a neighborhood relationship, and each neuron corresponds to a weight vector (Fig. 2). The iterative steps of SOM neural network training can be briefly described as follows (Kohonen, 1982, 1995; Kalteh et al., 2008).

(a) Initialize the weight vectors of neurons;

(b) Find the neuron corresponding to the weight vector that has the closest Euclidean distance to the input vector, called the winner neuron or Best Matching Unit (BMU);

(c) Update the weight vectors of the BMU and neighboring neurons according to the following rule to make them closer to the input vectors:

$$w_i(t+1) = w_i(t) + l(t)\,h_{ci}(r(t))[x(t) - w_i(t)], \quad (13)$$

where $w_i(t+1)$ and $w_i(t)$ are the weight vectors of the next iteration and the current iteration; $l(t)$ is the learning rate; $h_{ci}(r(t))$ is the neighborhood kernel around the BMU c_i; $r(t)$ is the neighborhood radius; $x(t)$ is the input vector.

The number of neurons in an SOM neural network is usually determined by the following equation (Vesanto et al., 2000):

$$n = 5\sqrt{N_s}, \quad (14)$$

where n is the number of neurons; N_s is the number of samples.

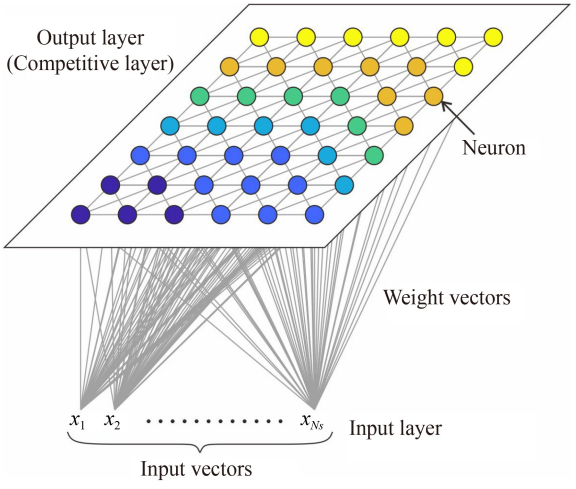

Fig. 2 Schematic diagram of SOM neural network structure.

The geological model parameters used for SOM neural network training are processed by min-max normalization:

$$x' = \frac{x - x_{\min}}{x_{\max} - x_{\min}}, \tag{15}$$

where x and x' are the original value and normalized value; $x_{\min}$ and $x_{\max}$ are the minimum value and the maximum value of the variables.

The SOM neural network training in this study can be regarded as data pre-processing, so fully converging is not necessary. Therefore, the number of iteration steps of the SOM neural network training in this study is set to 300.

3.5 *K*-means clustering algorithm

As an iterative clustering algorithm, the *K*-means clustering algorithm first requires specifying the number of clusters k; subsequently, k points within the data set are randomly selected as the initial centroids, and each data point is assigned to their closest centroid, forming the predefined k clusters. Then the mean of the data points within the cluster is calculated and used as the new centroid to start the next iteration until the centroids no longer change (MacQueen, 1967; Chen et al., 2017; Brentan et al., 2018; Santos et al., 2020). The main drawback of the K-means clustering algorithm is that the clustering result is highly dependent on the initial centroids. The weight vectors obtained by the SOM neural network training greatly reduce the sample size of the original data set and retain the original data characteristics. It is advantageous to use the K-means algorithm to cluster the weight vectors of the SOM neural network to avoid poor clustering results due to improper selection of the initial centroids (Chen et al., 2017; Santos et al., 2020).

This study refers to the Davies-Bouldin index (DBI) and elbow diagram method to determine k. The DBI could be calculated by (Davies and Bouldin, 1979)

$$\begin{cases} S_i = \left\{ \dfrac{1}{T_i} \displaystyle\sum_{j=1}^{T_i} \left| C_{ij} - A_i \right|^2 \right\}^{\frac{1}{2}} \\ M_{ij} = \left\{ \displaystyle\sum_{l=1}^{k} \left| a_{li} - a_{lj} \right|^2 \right\}^{\frac{1}{2}} \\ R_{ij} = \dfrac{S_i + S_j}{M_{ij}} \\ D_i = \max\limits_{j \neq i} R_{ij} \\ \mathrm{DBI} = \dfrac{1}{k} \displaystyle\sum_{i=1}^{k} D_i \end{cases}, \tag{16}$$

where S_i is the mean distance from the points in cluster i to the centroid; T_i is the number of points in cluster i; C_{ij} is the jth point in cluster i; A_i is the centroid of cluster i; M_{ij} is the distance between cluster i and cluster j; a_{li} is the value of the lth feature in the cluster center of cluster i; R_{ij} is used to measure the similarity between cluster i and cluster j; D_i is the maximum of the similarity between cluster i and the rest of clusters. The smaller the DBI, the better the clustering effect.

The Sum of Squared Errors (SSE) of the clustering results is an indicator of the elbow diagram method to determine k (Syakur et al., 2018), and it can be calculated as follows:

$$\mathrm{SSE} = \sum_{i=1}^{k} \sum_{C_{ij} \in C_i} \left| C_{ij} - A_i \right|^2. \tag{17}$$

As the k increases, the SSE will start to decrease and form a curve similar to the elbow. The optimal k corresponds to the position where the curve changes from steep to gentle (elbow).

The above SOM neural network and *K*-means clustering algorithms were implemented using the MATLAB SOM Toolbox (Vesanto et al., 2000).

3.6 Kruskal–Wallis test

The basic idea of the Kruskal–Wallis test is to mix multiple groups of samples and sort them in ascending order, assign ranks to the sorted data points, and compare the average ranks between groups to determine whether there is a significant difference. The statistic H of the Kruskal–Wallis test is defined as

$$H = \frac{12}{m(m+1)} \sum_{i=1}^{g} \frac{R_i^2}{m_i} - 3(m+1), \tag{18}$$

where g is the number of sample groups; m is the total sample size; m_i is the sample size of the ith group; R_i is the sum of the ranks in the ith group.

Given a significance level α and calculating the p-value of the statistic, if the p-value is less than α, the original hypothesis is rejected, indicating a significant difference between the groups.

3.7 Factor analysis

Factor analysis is a method of data dimensionality reduction that finds a set of nonlinearly correlated latent variables (factors) that represent the majority of the information in the original variables and highlights the relationship between factors and the original variables through the rotation of factor loadings.

The geological model parameters used for factor analysis are processed by Z-score normalization:

$$x' = \frac{x - x_{\text{mean}}}{\sigma}, \quad (19)$$

where x_{mean} is the mean of the variables; σ is the standard deviation of the variables.

The SPSS software was used to implement the Kruskal–Wallis test and factor analysis in this study.

4 Results and discussion

4.1 Structural model

The fault model (pillar) was constructed based on the seismic fault interpretation results (Fig. 3(a)). In the seismic survey area, faults are widely distributed, with 2 groups of fault systems primarily developed in the near north–south and north-west-south-east directions. Using the seismic interpretation results of coal seams as the trend and the coal seam data of drilling wells as constraints and corrections, the horizon models of Nos. 1, 4, 7, and 11 coal seams were established. Taking the horizon model of the No. 11 coal seam as an example (Fig. 3(b)), the study area is generally high in the north-west and low in the south-east, with 2 nose structures and 2 depressions. The western nose structure is larger in extent and dips to the east, while the eastern nose structure is smaller and dips to the north-west. The 2 nose structures are connected by a saddle, separating the 2 depressions. It should be noted that there is no fault data outside of the seismic survey area, and the horizon models were established only relying on the coal seam data from drilling wells, so it is smoother than that of the seismic survey area.

To avoid the invalid grid generated by the mismatch between the grid size and the distance between faults, the grid size is set to 30 m × 30 m, and a grid consistent with the fault strike was obtained (Fig. 3(c)). The model is subdivided into 59 layers vertically. Since Nos. 1, 4, and 7 coal seams are thin and contain 2–4 layers of coal body structures, and they were subdivided into 8 layers each (Figs. 4(a), 4(b), and 4(c)); the thicker No. 11 coal seam generally has more than 5 layers of coal body structures and contains some thin layers, so it was subdivided into 32 layers (Fig. 4(d)); the strata between the coal seams were simplified into 3 layers. Combining the fault model, horizon model, and grid, the final structural model is obtained, as shown in Fig. 3(d).

4.2 Facies model of coal body structures

The Nos. 1, 4, and 7 coal seams have similar distribution patterns of coal body structure types and proportions, primarily CC and GC, with a low thickness proportion of UC and rare MC (Figs. 4(a), 4(b), 4(c)). The coal body structure in the No. 11 coal seam is dominated by GC (Fig. 4(d)), indicating that the damage degree of the coal body structure in the No. 11 coal is significantly higher than that of the upper 3 coal seams. Coal, as a soft rock, is more prone to stress concentration than sandstone and limestone in the coal strata, and the greater the thickness of the coal seam, the more likely it is to suffer from stress concentration, leading to coal body structural damage (Guo et al., 2002; Ju et al., 2002; Wang et al., 2018; Liu et al., 2022). The thickness difference between the No.11 coal seam and the upper 3 coal seams could be the main reason for the differential distribution of coal body structures. The built-in "Most of" method in Petrel software was used to upscale the coal body structure in wells. The upscaling data matched well with the original data, the original distribution pattern was retained, and most of the thin layers did not disappear (Fig. 4).

Petrel software's built-in sequential indication algorithm was used to perform the stochastic simulation of the facies model of coal body structures, which is constrained by the distribution probability trend converted from the coal body structure thickness predicted from seismic attributes. Figure 5 shows 16 layers in the facies models of No. 1, 4, 7, and 11 coal seams. The distribution of CC and GC is more continuous in Nos. 1, 4, and 7 coal seams, whereas the distribution of UC is limited, and MC is developed sporadically (Fig. 5). The GC is continuous and widespread in the No. 11 coal seam, the distribution of UC and CC is relatively limited, and the continuity of MC is slightly better than in the Nos. 1 and 4 coal seams. The coal body structure frequently varies between layers in the 4 coal seams, as evidenced by the vertical distribution of coal body structures (Fig. 4).

4.3 Property models of permeability and gas content

4.3.1 Permeability and gas content

Table 1 lists the parameters for determining permeability using the production performance analysis method (Shi et al., 2018, 2019, 2020). Figure 6 shows the results of determining the permeability of coal reservoirs for 2 CBM wells using the production performance analysis method. The daily water production in the early CBM development should be discarded due to its low and rapidly changing (Shi et al., 2018). The casing pressure of wells Z1 and Z1-4-X8 appeared on days 44 and 30, respectively (Figs. 6(a) and 6(b)), indicating the end of the single-phase water flow stage. Days 15 to 38 for well Z1 and days 7 to 30 for well Z1-4-X8 were chosen to fit the data, and good fitting results were obtained, with R^2 coefficients greater than 0.99. The slope of the fitted straight line of well Z1 is 0.6185 MPa·d/m^3 (Fig. 6(c)), and the coal seam thickness is 4.37 m; the reservoir permeability is 0.681 mD according to Eq. (9), which is a typical high permeability reservoir in the study area; substituting the intercept −0.6546 MPa·d/m^3 into Eq. (10) yields a skin factor of −0.655. Substituting the slope of

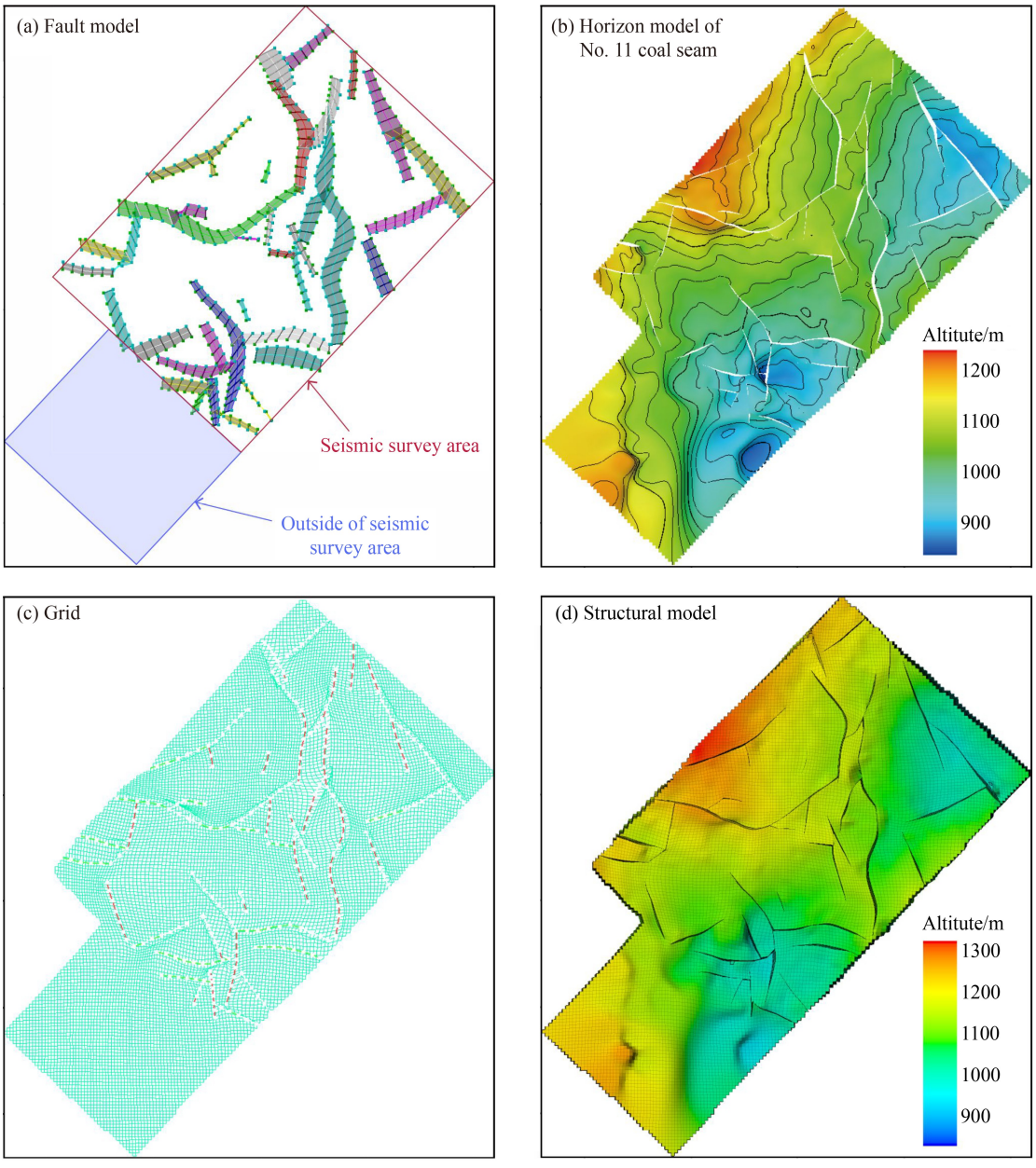

Fig. 3 Establishment of the structural model in the study area.

the fitted straight line (0.5433 MPa·d/m^3) and the coal seam thickness (10.03 m) of well Z1-4-X8 into Eq. (9) yields a reservoir permeability of 0.338 mD, which is typical of low-permeability reservoirs in the study area; substituting the intercept of −0.0955 MPa·d/m^3 into Eq. (10) yields a skin factor of −0.176. Both wells have skin factors less than 0, suggesting that hydraulic fracturing has improved the reservoir permeability performance near the wellbore.

The weak negative correlation between the thickness proportion of UC and permeability corresponds to the relatively low permeability of UC despite having the primary cleat system (Fig. 7(a)). The significant positive correlation between the thickness proportion of CC and permeability implies that the CC suffered brittle damage as a result of stress, and secondary fractures were further extended in the primary cleat system, resulting in significantly higher permeability than the UC (Fig. 7(b)) (Fu et al., 2009; Liu et al., 2015; Li et al., 2019). There is a negative correlation between the thickness proportion of GC and permeability (Fig. 7(c)), which is due to the significantly lower permeability as a result of ductile deformation of GC after enduring higher tectonic stresses (Fu et al., 2009; Pan et al., 2016; Li et al., 2017a; Li et al., 2019; Cheng and Pan, 2020). The negative correlation between the thickness proportion of MC and permeability corresponds to a more fragmented coal body structure of the MC (Fig. 7(d)). The least-squares solution of the overdetermined equations involving the permeability and thickness proportion of coal body structures reveals that

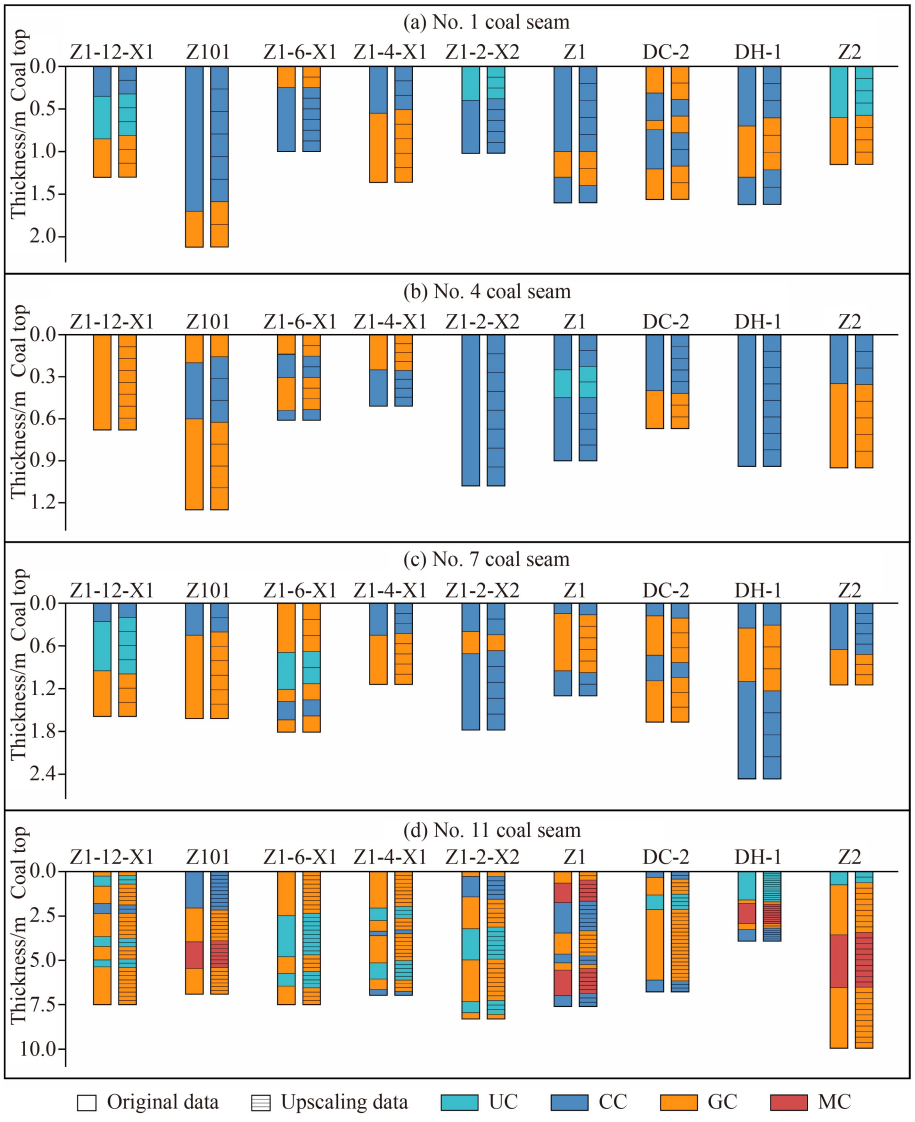

Fig. 4 Vertical distribution and upscaling of coal body structures (the profile location is the green line in Fig. 1(d)).

the *in situ* permeability of UC, CC, GC, and MC is 0.333 mD, 0.931 mD, 0.146 mD, and 0.099 mD, respectively. The permeability of CC is 6.38 times and 9.40 times higher than that of GC and MC, respectively.

The damage degree of coal body structures is negatively related to density, positively related to Langmuir volume, and insignificantly related to Langmuir pressure (Fig. 8). The secondary fractures increase as the damage degree of coal body structures increases, and the coal tends to loosen, resulting in a decrease in density, while the adsorption capacity for methane increases due to the rise in microporous volume and surface area (Fu et al., 2009; Skoczylas et al., 2014; Zhang et al., 2017; Cheng and Pan, 2020). In the isothermal adsorption experiment, coal samples with different coal body structures all need to be made into particles, destroying the coal microstructure, which could be the reason for the insignificant differences in the Langmuir pressure between different coal body structures (Cheng and Pan, 2020). Assuming that the density, Langmuir volume, and Langmuir pressure of the 4 coal body structures are the average values of the tested samples, the gas saturation is 0.9, and the coal gas content was calculated using Eq. (12). When the masses are equal, the gas content of CC, GC, and MC is 0.98 times, 1.27 times, and 1.37 times of that of UC, respectively. The TDC shows an obvious gas-bearing advantage.

4.3.2 Property models of permeability and gas content

The facies-controlled method was used for reservoir permeability and gas content property modeling. 2 layers in property models for each of the 4 coal seams are shown in Fig. 9, and the permeability and gas content models are in the left and right columns, respectively. The high-permeability low-gas content area overlaps with UC and CC distribution areas, and the low-permeability high-gas content area mainly corresponds to the TDC

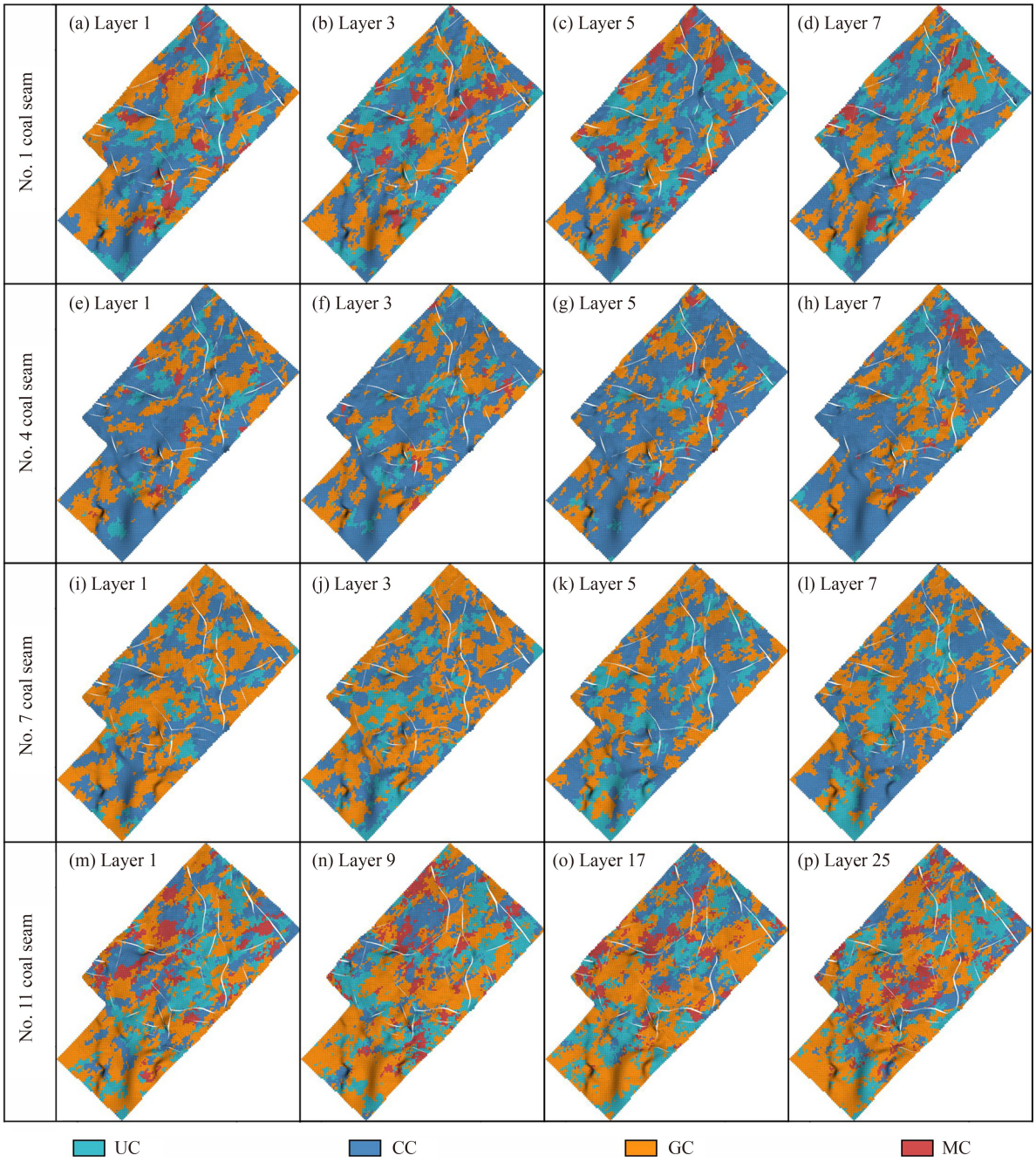

Fig. 5 Facies model of coal body structures.

Table 1 Parameters for determining permeability using the production performance analysis method

Parameters	Value	Unit	Sources
Water viscosity (μ_w)	1	mPa·s	Shi et al. (2018, 2019, 2020)
Water formation volume factor (B_w)	1		
Reservoir porosity (φ)	0.03		
Total compressibility（C_t）	0.02	MPa^{-1}	
Half-length of hydraulic fracture（L_f）	100	m	Microseismic monitoring of hydraulic fracture

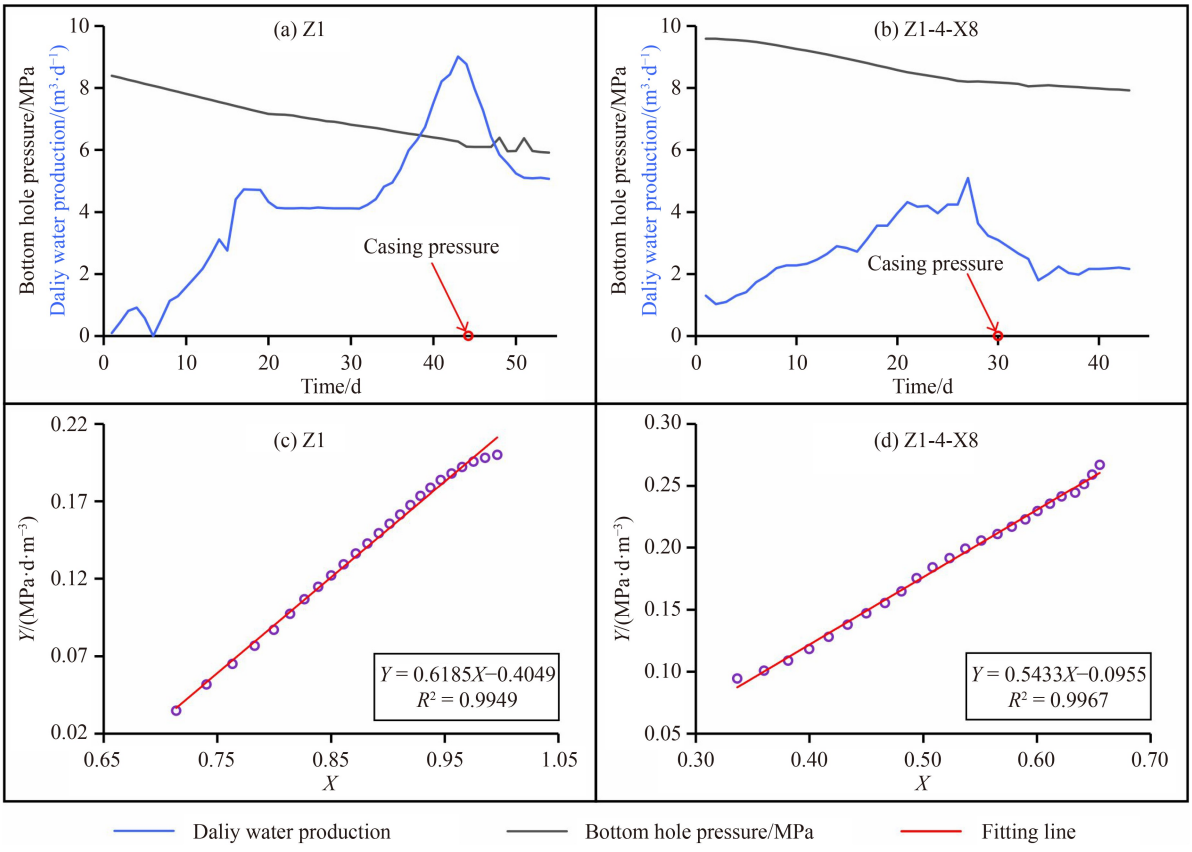

Fig. 6 The results of permeability determination using the production performance analysis method.

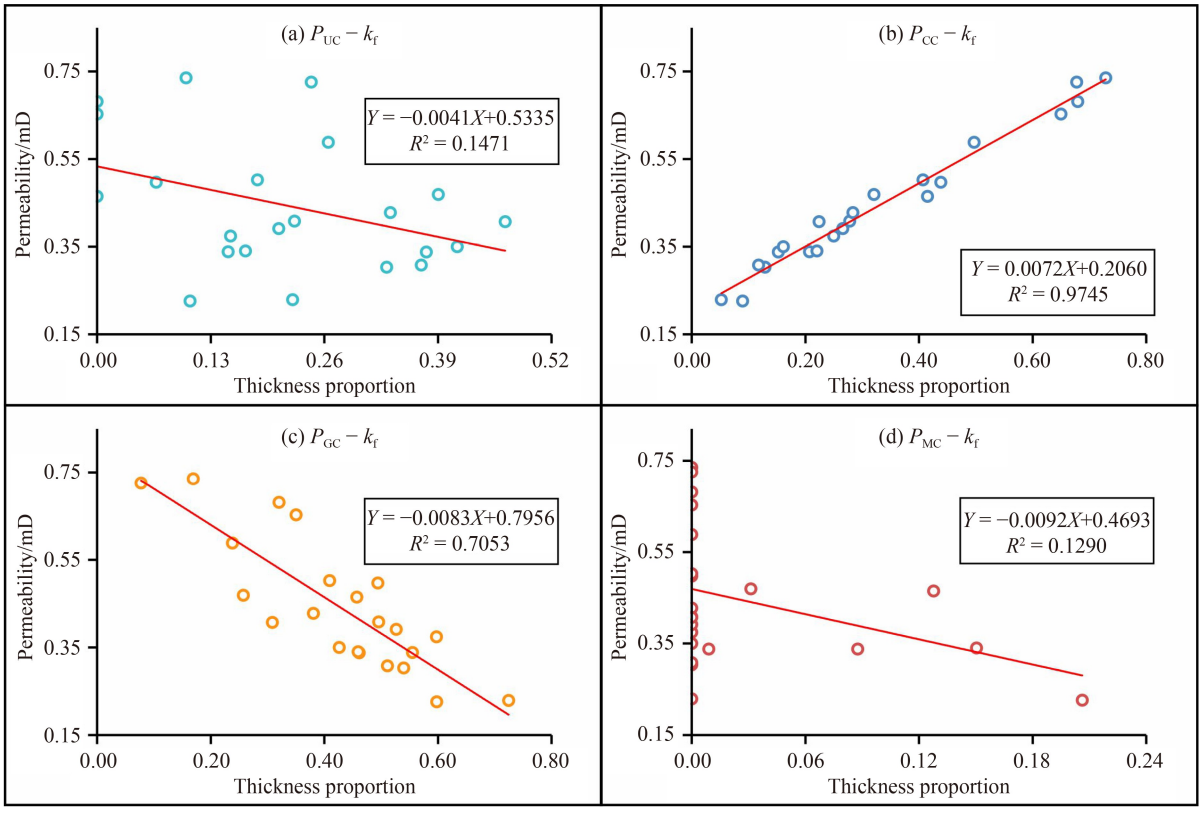

Fig. 7 Relationships between permeability and the thickness proportion of coal body structures.

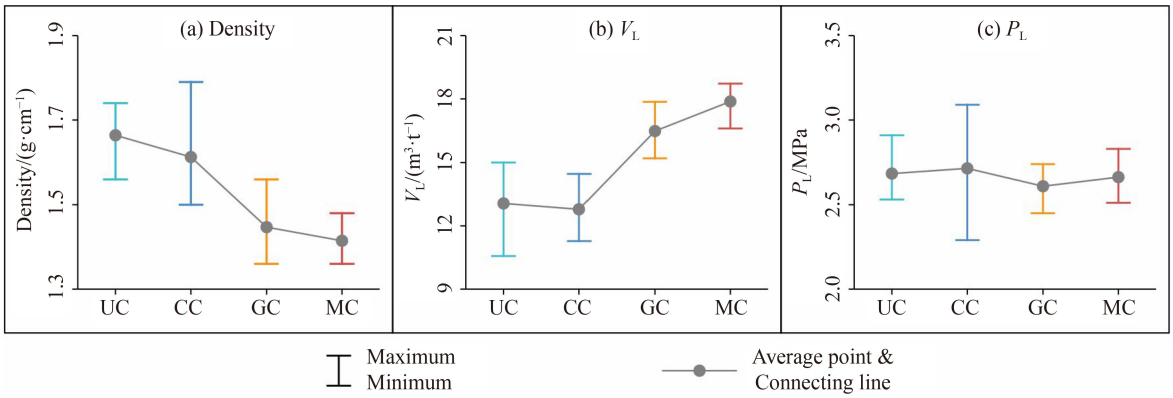

Fig. 8 Coal sample test results of density, Langmuir volume, and Langmuir pressure.

reservoirs distribution area (Fig. 5; Fig. 9). The high-permeability areas in the Nos. 1, 4, and 7 coal seams are more continuous and widespread as the CC develops, but the gas content is poor. The TDC reservoirs are widely developed in the No. 11 coal seam, despite its higher gas content, the overall permeability is low, and the high-permeability areas are discontinuously distributed (Fig. 9). The reservoir permeability largely determines the production of CBM wells, and the continuous TDC low-permeability area is not conducive to CBM development. The above analysis reveals the reasons for the low production of some wells in the study area with the thicker No. 11 coal seam as the target layer and higher production with thinner Nos. 1, 4, and 7 coal seams for multi-layer development, reflecting the constraints of coal body structure on CBM production.

4.4 Results of SOM neural network and *K*-means clustering

The 30 variables (model parameters) used as inputs to the SOM neural network are listed in Table 2. The permeability and gas content are weighted averages calculated based on the thickness proportion of coal body structures. The geological model parameters were gridded with a grid size of 100 m × 100 m, and the parameter values of the grid vertices were collected as the data set, totaling 1097 sample points. The number of neurons is $5\sqrt{1097}\approx 166$ according to Eq. (14), and the grid size of the SOM neural network is a 14 × 12 asymmetric structure to avoid the effect of boundary effects (Fig. 10) (Kohonen, 1982; Chen et al., 2017).

The unified distance matrix (U-Matrix) of the SOM neural network reflects the distances between a neuron and its neighbors. The distance between a neuron and a neighboring neuron is represented by the color of the hexagon between them, and the color of a neuron represents its average distance from all neighboring neurons (Fig. 10(a)). The high value (yellow) hexagon in U-Matrix reflects the large difference between adjacent neurons. When k is 6, the *DBI* reaches a minimum, and the *SSE* curve is at the elbow position, indicating that the k setting of 6 is appropriate (Fig. 10(b); Fig. 11). Comparing the U-Matrix with the *K*-means clustering result (Fig. 10), the neurons in the area corresponding to clusters 1, 4, and 5 in the U-Matrix have large differences with neighboring neurons, so the *K*-means algorithm classifies them into 3 clusters. The remaining area in the U-Matrix shows a smooth variation that is difficult to divide from the visualization, and the algorithm further classifies it into 3 clusters, manifesting the necessity of applying the *K*-means clustering algorithm.

The component planes of the SOM neural network show the statistical distribution pattern of the variables. Similar to Fig. 10(a), yellow and blue represent the high and low values of the variables (Fig. 12). Similar color distributions between the component planes represent positive correlations between variables, while the opposite indicates negative correlations. As mentioned in Section 4.2, the types and proportions of coal body structures in Nos. 1, 4, and 7 coal seams are similar in terms of vertical distribution (Fig. 4), which is also shown in the component planes. There are weak positive correlations between the UC thickness proportions of Nos. 1 and 4 coal seams, between the CC thickness proportions of Nos. 1 and 7 coal seams, and between the MC thickness proportions of Nos. 1 and 4 coal seams (Fig. 12). The correlations between the component planes of the thickness proportion of coal body structure of the No. 11 coal seam and the other 3 coal seams are low, indicating the different coal body structure distribution pattern and genesis mode of the No. 11 coal seam and the other 3 coal seams. The permeability/gas content is positively/negatively correlated with the thickness proportion of CC, and negatively/positively correlated with the proportion of GC because they are weighted averages (Fig. 12).

There are positive correlations between the thicknesses of Nos. 1, 4, 7, and 11 coal seams, with the thickness correlation between Nos. 7 and 11 coal seams being the most significant (Fig. 12). The spacing between Nos. 1 and 4 coal seams is weakly negatively correlated with the

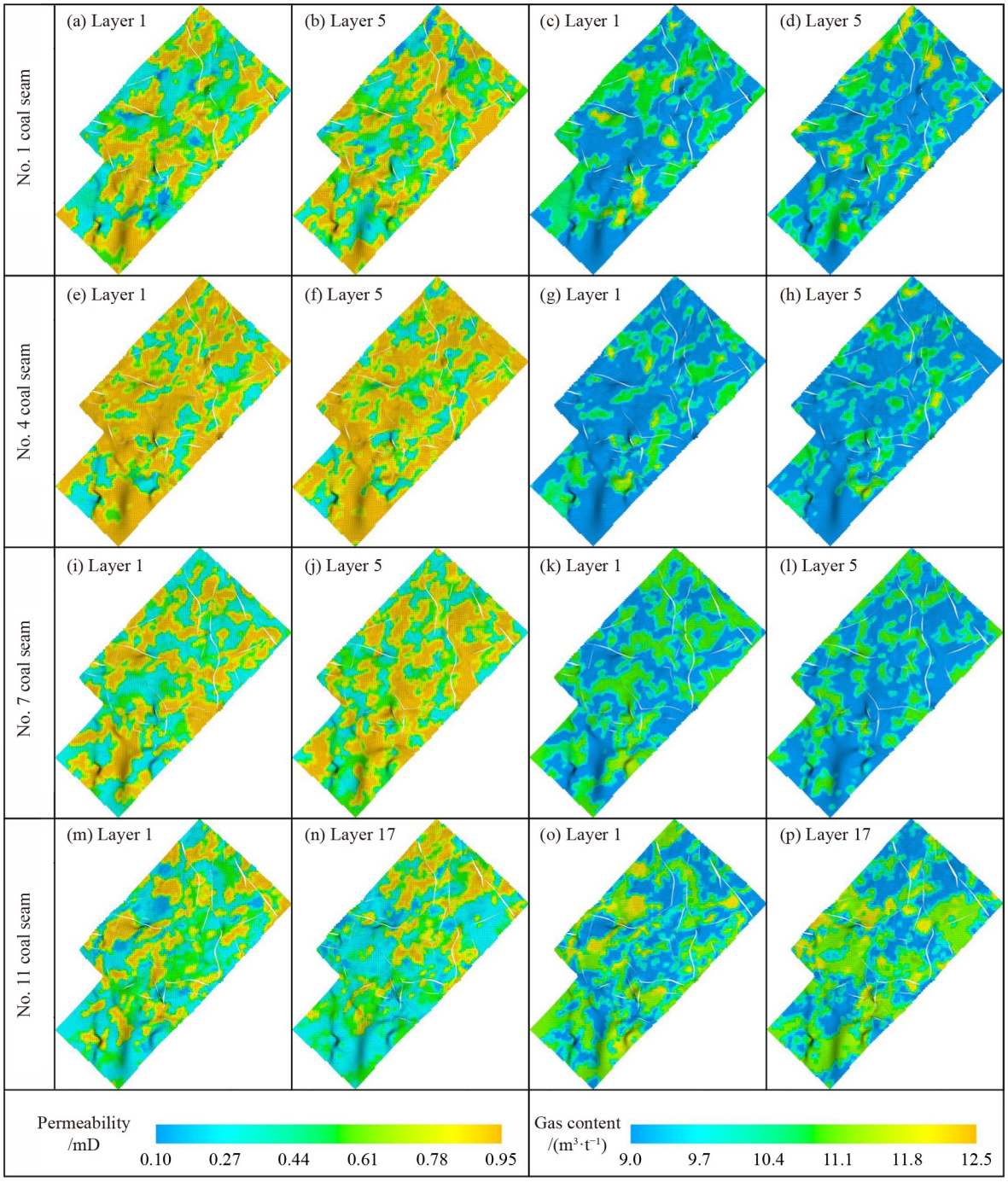

Fig. 9 Property models of permeability and gas content.

Table 2 Input variables of SOM neural network

Variables	Variable description	Dimension
Thickness proportion of coal body structure	4 types of coal body structure in Nos. 1, 4, and 11 coal seams, 3 types of coal body structure in the No. 7 coal seam	15
Permeability	Nos. 1, 4, 7, and 11 coal seams	4
Gas content	Nos. 1, 4, 7, and 11 coal seams	4
Thickness	Nos. 1, 4, 7, and 11 coal seams	4
Coal seam spacing	No. 1–No. 4, No. 4–No. 7, No. 7–No. 11	3

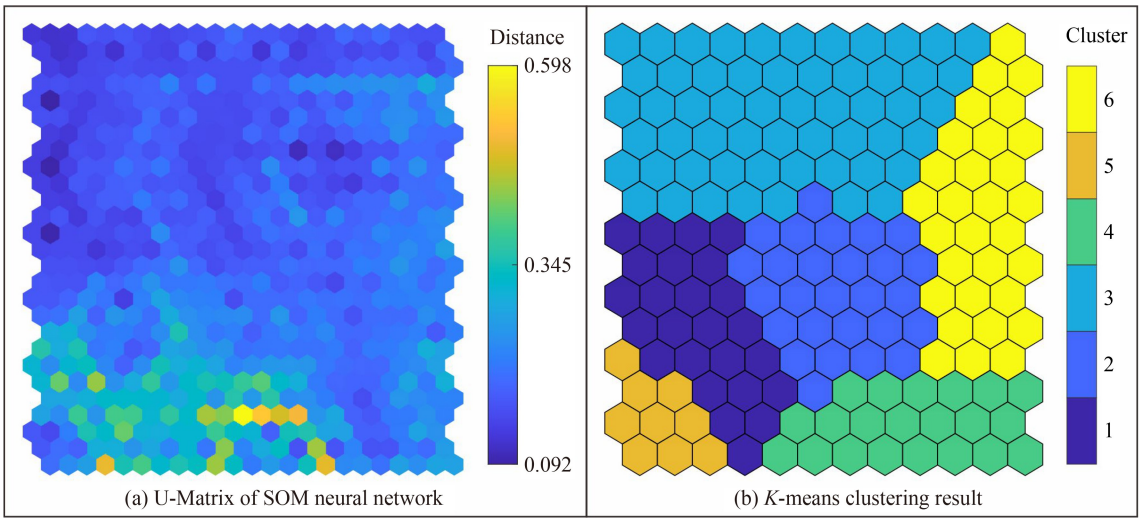

Fig. 10 SOM neural network and *K*-means clustering results.

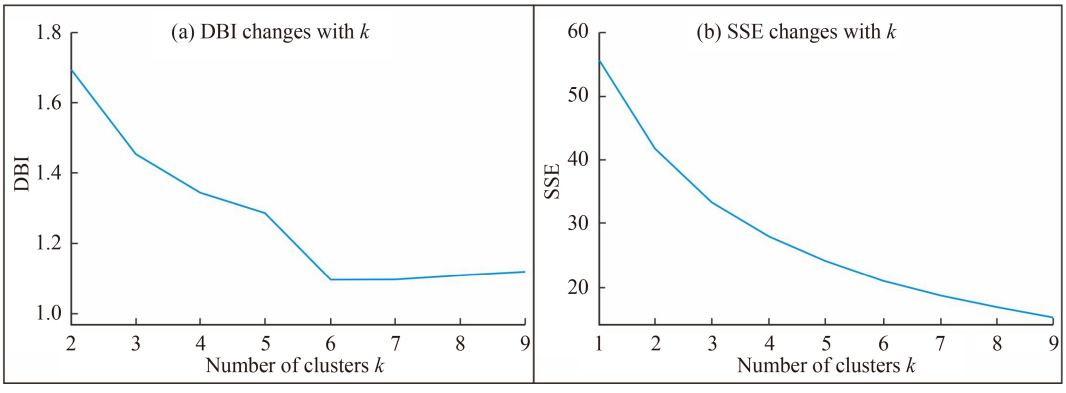

Fig. 11 Determination of the clusters number *k* of *K*-means clustering.

spacing between Nos. 4 and 7 coal seams, and their variation ranges are larger. The spacing between Nos. 7 and 11 coal seams is more stable. The depositional environment is an important factor contributing to the differences in coal seam thickness and spacing. The Late Permian coal strata in the study area were formed in a transgressive depositional system (Wang et al., 2011; Shen et al., 2012). Nos. 7 and 11 coal seams belong to the early transgressive sequence (the top and bottom boundaries are the K3 limestone and No. 14 coal seam), which corresponds to the overall rapid rise stage of sea-level; due to the similar depositional environment, the thickness correlation between coal seams is strong and the coal seam spacing is stable. Nos. 1 and 4 coal seams belong to the late highstand sequence (the top boundary is the top of the Upper Permian, and the bottom is the K3 limestone), and the sea-level rise rate slowed down and reached the maximum sea flood surface; the coal seam deposition was influenced by tidal action, resulting in a lower thickness correlation with the earlier deposited coal seams and the coal seam spacing is no longer stable.

The planar distribution of the 6 clusters in the study area is shown in Fig. 13. The distribution of clusters is more continuous in the fault-less developed area, whereas in the fault-dense area, different clusters cross each other with less continuity. Constrained by the density of the well pattern, the cluster distribution in the area outside of the seismic survey area is simpler and more continuous. It should be noted that cluster 5 is only found outside of the seismic survey area, which may indicate a bias in statistical analysis.

4.5 Data analysis of the geological model

Table 3 shows the results of the Kruskal–Wallis test, and *p*-values less than 0.001 are approximated by 0. Assign significance level α as 0.01. The *p*-values of the vast majority of variables are less than 0.01, indicating that the model parameters differ significantly between clusters, which supports the *K*-means clustering results. The *p*-values of the spacing between Nos. 7 and 11 coal seams among different clusters are generally greater than 0.01, indicating no statistically significant differences between clusters, which is consistent with the previously mentioned results that the spacing between Nos. 7 and 11 coal seams is more stable (Fig. 12).

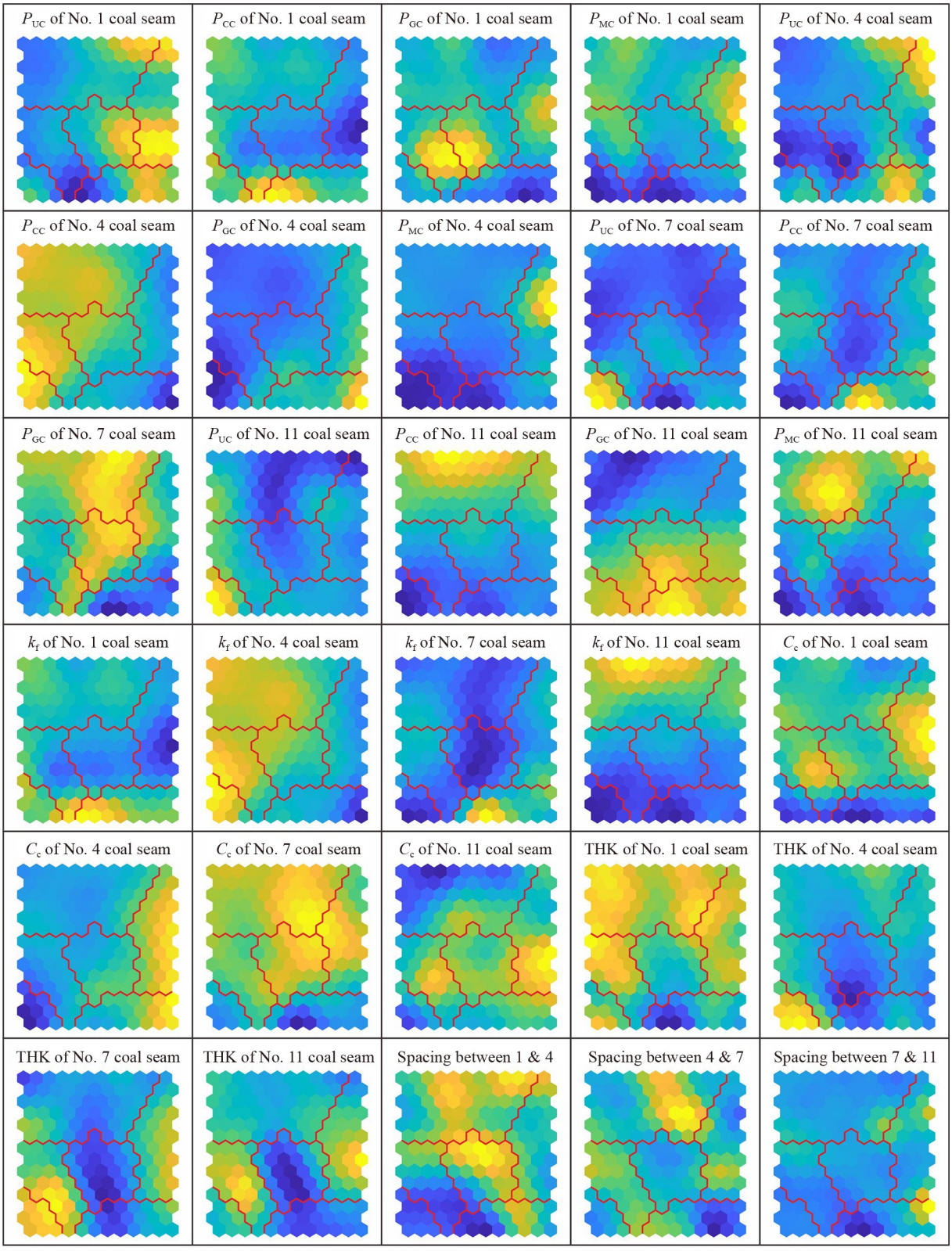

Notes: THK is the abbreviation of thickness; "Spacing between *m* & *n*" means the spacing between Nos. *m* and *n* coal seams.

Fig. 12 Component planes of SOM neural network.

Many variables with complex data distribution characteristics are involved in the data analysis. Because of the strong correlations between the thickness proportion of coal body structures and coal reservoir permeability and gas content, they can be analyzed uniformly. As the spacing between Nos. 7 and 11 coal seams is similar

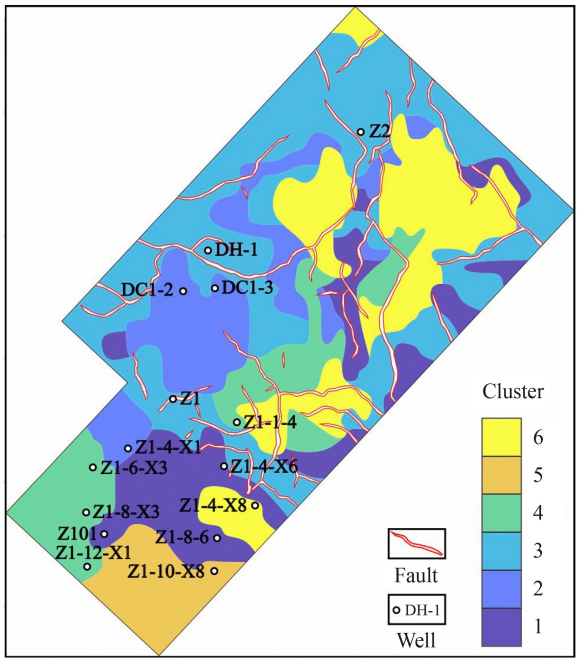

Fig. 13 Planar distribution of the clusters.

between clusters, it could be ignored in the analysis of data differences. To facilitate the interpretation of the data characteristics, factor analysis was conducted for the variables except for the thickness proportion of coal body structures and the spacing between Nos. 7 and 11 coal seams (Table 4). The positive and negative factor loadings represent the correlation of the variables with the factors. The results of factor analysis show that 4 property factors are extracted from the permeability and gas content of Nos. 1, 4, 7, and 11 coal seams. The property factors of Nos. 1 and 7 coal seams are negatively correlated with permeability and positively correlated with gas content, while the property factors of Nos. 4 and 11 coal seams are the opposite. The thicknesses of 4 coal seams have large positive factor loadings on the thickness factor. The spacing factor shows higher factor loadings for the spacing between Nos. 1 and 4 coal seams and the spacing between Nos. 4 and 7 coal seams, and it is negatively correlated with the former and positively correlated with the latter.

Figures 14 and 15 show the box plots of different clusters of variables and factors. The blue box is the interquartile range (IQR); the blue dots within the IQR box represent the median; and the T-shaped blue lines extending above and below the IQR box represent the interval of normal data, with the distance between its upper and lower limits to the IQR being generally 1.5 times the IQR length. When no outliers (red dots) exceed this interval, the interval is replaced by the maximum and minimum values of the variables. The relatively thin IQRs and fewer outliers in Figs. 14 and 15 indicate a concentrated data distribution. It should be noted that while the factors are somewhat representative of the trends in the original variables, there can be inconsistent trends, which are more noticeable when the absolute values of the factor loadings are low.

The median is used as an indicator to analyze the model parameter characteristics of the clusters. The medians of all 4 property factors of cluster 1 are at medium levels (Fig. 15), indicating that the permeability and gas content of all 4 coal seams are at medium levels between clusters, and corresponding to the thickness proportions of CC and GC are not prominent (Fig. 14). The higher medians of thickness factor and spacing factor indicate that the 4 coal seams are thicker, the spacing between Nos. 1 and 4 coal seams is smaller, while the spacing between Nos. 4 and 7 coal seams is larger (Fig. 14; Fig. 15).

For cluster 2, the median of the property factor of the No. 7 coal seam is the highest among different clusters (Fig. 15), indicating that the No. 7 coal seam has lower permeability and higher gas content, that is, the thickness proportion of CC is lower while the thickness proportion of GC is higher (Fig. 14). The medians of thickness factor and spacing factor are the lowest among different clusters (Fig. 15), suggesting that the 4 coal seams are thinner, and the spacing between Nos. 1 and 4 coal seams is larger, while the spacing between Nos. 4 and 7 coal seams is smaller (Fig. 14).

The medians of property factors of cluster 3 for Nos. 1, 4, and 7 coal seams are all at medium levels among different clusters (Fig. 15), indicating that their reservoir permeability and gas content are all at medium levels; the No. 7 coal seam has a higher gas content, corresponding to a higher thickness proportion of GC (Fig. 14). The median of the property factor of the No. 11 coal seam is the highest among different clusters (Fig. 15), showing that the No. 11 coal seam has higher permeability and lower gas content, which corresponds to a higher thickness proportion of CC and a lower thickness proportion of GC (Fig. 14). The medians of thickness factor and spacing factor are at medium levels among different clusters (Fig. 15), representing that the related model parameters are all at medium levels (Fig. 14).

The medians of the 4 property factors of cluster 4 are relatively lower (Fig. 15), indicating that among the different clusters, Nos. 1 and 7 coal seams have higher permeability and lower gas content, while Nos. 4 and 11 coal seams have lower permeability and higher gas content (Fig. 14). The lower median of the thickness factor indicates that all 4 coal seams are thinner (Fig. 14 and Fig. 15). Although the median of the spacing factor is in the medium level among different clusters (Fig. 15), the spacing between Nos. 1 and 4 coal seams and spacing between Nos. 4 and 7 coal seams are actually smaller (Fig. 14).

The medians of the property factors of Nos. 1 and 4 coal seams in cluster 5 are the lowest and highest among different clusters, respectively (Fig. 15), indicating the

Table 3 The *p*-value of the Kruskal-Wallis test

Variables	1–2	1–3	1–4	1–5	1–6	2–3	2–4	2–5	2–6	3–4	3–5	3–6	4–5	4–6	5–6
P_{UC} of No. 1 coal seam	0	0	0	0	0	0	0.066	0.003	0.001	0.008	0.735	0	0.145	0	0
P_{CC} of No. 1 coal seam	0	0.807	0	0	0	0	0	0	0.013	0	0	0	0.998	0	0
P_{GC} of No. 1 coal seam	0.098	0	0	0	0.654	0	0	0	0.031	0	0.027	0	0	0	0
P_{MC} of No. 1 coal seam	0.018	0.164	0	0	0.013	0	0	0	0	0	0	0.126	0	0	0
P_{UC} of No. 4 coal seam	0	0	0	0	0	0.357	0	0.193	0	0	0.431	0	0	0.324	0.002
P_{CC} of No. 4 coal seam	0	0.017	0	0.001	0	0	0	0	0	0	0	0	0	0.273	0
P_{GC} of No. 4 coal seam	0	0.652	0	0	0	0	0	0	0	0	0	0	0	0.202	0
P_{MC} of No. 4 coal seam	0.708	0	0	0.608	0	0	0.394	0	0	0	0	0	0	0	0
P_{UC} of No. 7 coal seam	0	0.019	0.386	0	0.474	0	0	0	0	0.002	0	0.103	0	0.807	0
P_{CC} of No. 7 coal seam	0	0	0	0	0.009	0	0	0.100	0	0	0	0	0	0.002	0
P_{GC} of No. 7 coal seam	0	0	0	0	0.142	0.281	0	0	0	0	0	0	0.746	0	0
P_{UC} of No. 11 coal seam	0	0	0	0	0	0.004	0	0	0.001	0.003	0	0.298	0	0.062	0
P_{CC} of No. 11 coal seam	0.001	0	0	0.013	0	0	0	0	0	0	0	0	0	0	0
P_{GC} of No. 11 coal seam	0.001	0	0	0	0.004	0	0.001	0.088	0	0	0	0	0.325	0	0
P_{MC} of No. 11 coal seam	0.091	0	0	0	0.153	0	0	0	0.002	0	0	0	0.004	0	0
k_f of No. 1 coal seam	0	0.466	0	0	0	0	0	0	0.029	0	0	0	0.839	0	0
k_f of No. 4 coal seam	0	0.037	0	0	0	0	0	0	0	0	0	0	0	0.398	0
k_f of No. 7 coal seam	0	0	0	0	0.016	0	0	0.628	0	0	0	0	0	0	0
k_f of No. 11 coal seam	0.070	0	0	0	0	0	0	0	0	0	0	0	0.005	0	0
C_c of No. 1 coal seam	0.234	0.001	0	0	0	0.066	0	0	0	0	0	0	0.505	0	0
C_c of No. 4 coal seam	0	0.402	0	0	0	0.001	0	0	0	0	0	0	0	0	0
C_c of No. 7 coal seam	0	0	0	0	0.028	0.897	0	0	0.002	0	0	0	0.509	0	0
C_c of No. 11 coal seam	0.09	0	0	0.538	0.002	0	0.028	0	0.197	0	0.145	0	0	0	0
THK of No. 1 coal seam	0	0.858	0	0	0.043	0	0.002	0.031	0	0	0	0.008	0	0	0.026
THK of No. 4 coal seam	0	0.862	0	0	0.182	0	0.006	0	0	0	0	0.151	0	0	0
THK of No. 7 coal seam	0	0	0	0.002	0.552	0	0	0	0	0.838	0	0	0	0	0
THK of No. 11 coal seam	0	0	0	0	0.006	0	0.776	0	0	0	0.468	0	0	0	0
Spacing between 1 & 4	0	0	0	0.765	0.005	0.038	0	0	0	0	0	0.004	0	0.003	0
Spacing between 4 & 7	0	0.011	0	0	0	0	0.669	0.228	0.001	0	0	0.016	0.395	0	0
Spacing between 7 & 11	0.535	0.297	0.215	0.349	0.067	0.787	0.134	0.092	0.262	0.040	0.039	0.268	0.630	0.007	0.009

Notes: "*m*–*n*" means clusters *m* and *n*; double underscores indicate the *p*-value is higher than 0.01; THK is the abbreviation of thickness; "Spacing between *m* & *n*" means the spacing between Nos. *m* and *n* coal seams.

higher permeability and lower gas content of Nos. 1 and 4 coal seams (Fig. 14). Despite the fact that the medians of the property factors of Nos. 7 and 11 coal seams are at medium levels and the lowest among different clusters, respectively, indicating that the permeability and gas content of the No. 7 coal seam are at medium levels, and the lower permeability and higher gas content of the No. 11 coal seam (Fig. 15). The absolute values of the factor loadings for gas content are lower (Table 4). The permeability and gas content of Nos. 7 and 11 coal seams are actually lower among different clusters, which is due to the higher thickness proportion of UC with lower permeability and gas content (Fig. 14). The median of the thickness factor is the highest among different clusters, indicating that all 4 coal seams are thicker (Fig. 14 and Fig. 15), but Nos. 1 and 11 coal seams are actually thinner (Fig. 14), corresponding to lower factor loadings (Table 4). The lower median of the spacing factor indicates that the spacing between Nos. 1 and 4 coal seams is larger, while the spacing between Nos. 4 and 7 coal seams is smaller (Fig. 15); however, the spacing between Nos. 1 and 4 coal seams is also found to be smaller from Fig. 14.

For cluster 6, the medians of property factors of Nos. 1 and 4 coal seams are the highest and lowest among different clusters (Fig. 15), indicating that Nos. 1 and 4 coal seams have lower permeability and higher gas content, corresponding to the higher thickness proportion

Table 4 Rotated factor loadings

Variables	Property factor of No. 1 coal seam	Property factor of No. 4 coal seam	Property factor of No. 7 coal seam	Property factor of No. 11 coal seam	Thickness factor	Spacing factor
k_f of No. 1 coal seam	−0.821	0.105	−0.098	0.019	−0.057	0.140
C_c of No. 1 coal seam	0.911	−0.071	0.078	0.070	0.144	0.135
k_f of No.4 coal seam	0.053	0.956	0.100	0.071	0.094	0.109
C_c of No. 4 coal seam	0.295	−0.939	−0.036	−0.027	−0.046	0.033
k_f of No. 7 coal seam	0.051	−0.156	−0.922	0.028	0.014	0.113
C_c of No. 7 coal seam	0.387	−0.050	0.811	0.209	0.031	0.168
k_f of No. 11 coal seam	0.128	−0.036	0.128	0.933	−0.002	0.038
C_c of No. 11 coal seam	0.494	−0.216	0.085	−0.675	−0.070	0.089
THK of No. 1 coal seam	0.173	0.129	0.265	0.359	0.555	−0.032
THK of No. 4 coal seam	−0.293	0.185	0.092	0.141	0.716	−0.119
THK of No. 7 coal seam	0.106	−0.099	−0.272	−0.119	0.736	0.085
THK of No. 11 coal seam	0.332	0.050	0.061	−0.123	0.680	0.210
Spacing between 1 & 4	0.240	0.092	0.134	0.372	−0.201	−0.589
Spacing between 4 & 7	0.117	0.116	0.063	0.119	−0.015	0.851

Notes: double underscores indicate the absolute value of the factor loading is higher than 0.4; THK is the abbreviation of thickness; "Spacing between *m* & *n*" means the spacing between Nos. *m* and *n* coal seams.

of GC and the lower thickness proportion of CC. The medians of the property factors of Nos. 7 and 11 coal seams are at medium levels among different clusters (Fig. 15), indicating the permeability of Nos. 7 and 11 coal seams are at medium levels, but the gas content is actually higher (Fig. 14). The medians of the thickness factor and spacing factor indicate that the related model parameters are at medium levels among different clusters (Figs. 14 and 15). Based on the above analysis results, the model parameter characteristics of the 6 clusters are summarized as shown in Table 5.

4.6 Model applications and prospects

Geological modeling of CBM reservoirs in the TDC seam group and its data analysis are of significant reference for the multi-layer CBM co-development (Fig. 16(a)). The most commonly adopted CBM development method in southern China at present is "hydraulic fracturing and multi-layer CBM development" in vertical wells (Qin et al., 2018; Yang et al., 2018; Guo et al., 2020) (Fig. 16(b)). Taking the multi-layer CBM development in the study area as an example, the No. 11 coal seam is almost the mandatory production layer for multi-layer CBM development due to its thickness and resource advantage. However, due to the highly developed TDC reservoirs in the No. 11 coal seam, the hydraulic fracturing effect is often poor and also faces the influence of permeability stress-sensitive and velocity-sensitive during CBM development. If trying to avoid the above-mentioned problems to some extent, the cluster 3 with a lower thickness proportion of TDC reservoirs in the No. 11 coal seam is a more ideal choice.

Although the "hydraulic fracturing and multi-layer CBM development" in vertical wells could mobilize larger resources in the coal seam group, it is still less effective in the development of "low permeability and low mechanical strength" TDC reservoirs (Zhao et al., 2014; Ahamed et al., 2019; Sang et al., 2020; Song et al., 2021). The strong stress-sensitivity of TDC reservoirs is suitable for CBM development using stress-relief methods (Sang et al., 2010, 2020; Yuan, 2015; Wang et al., 2020). Stress-relief CBM development through the protective layer mining refers to triggering the "stress-relief, reservoir pressure reduction, and permeability increase" in the protected layer, which is TDC developed and prone to outburst, through coal mining in the adjacent protective layer, and the CBM is extracted by drilling wells in the stress-relief zone (Huang et al., 2010; Xu et al., 2011; Yang et al., 2011; Yuan, 2015) (Fig. 16(c)). Stress-relief CBM development through the protective layer mining is one of the most representative methods to achieve the co-development of coal and CBM in the coal seam group. Parameters such as coal body structure, thickness, and coal spacing are important parameters to be considered for the method (Yang et al., 2011; Wang et al., 2020). Geological modeling of CBM reservoirs in the TDC seam group and its data analysis are helpful in determining the protective layer (TDC not developed) and the protected layer (TDC developed), and further predict the protection range and effect. For instance, the coal seams of cluster 4 are smaller in spacing, Nos. 1 and 7 coal seams with higher permeability and low risk of outburst are suitable as protective layers, and Nos. 4 and

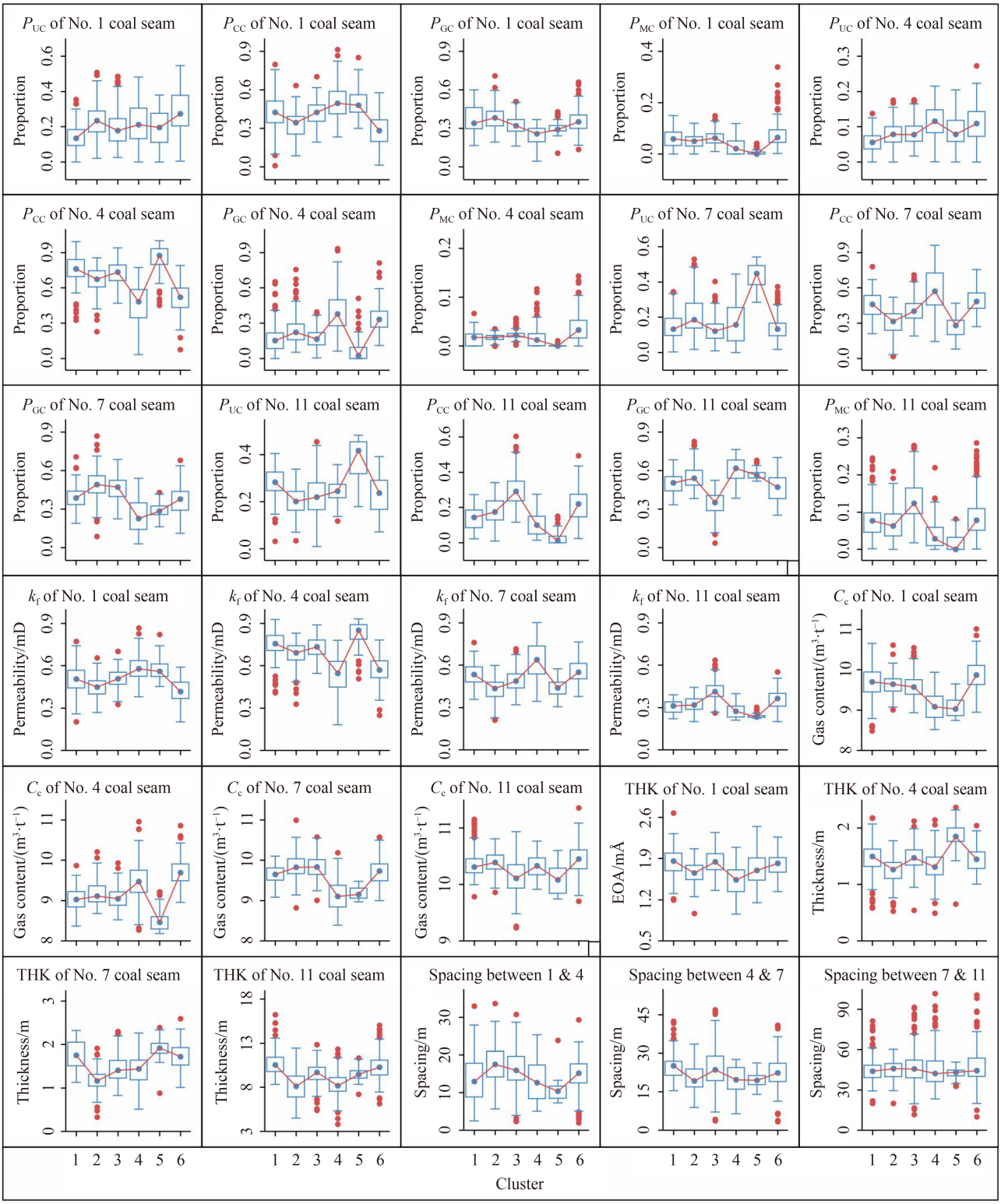

Notes: THK is the abbreviation of thickness; "Spacing between *m* & *n*" means the spacing between Nos. *m* and *n* coal seams.

Fig. 14 Box plots of different clusters of variables.

11 coal seams with low permeability are suitable as protected layers. But when the protective layer is located above the protected layer, the stress-relief effect may be poor. The method is limited to the coal mine area, and there are also disadvantages, such as the easy deformation and even breaking out of the preset wellbore and the short production period (Huang et al., 2010; Xu et al., 2011).

Taking advantage of the long extension of horizontal

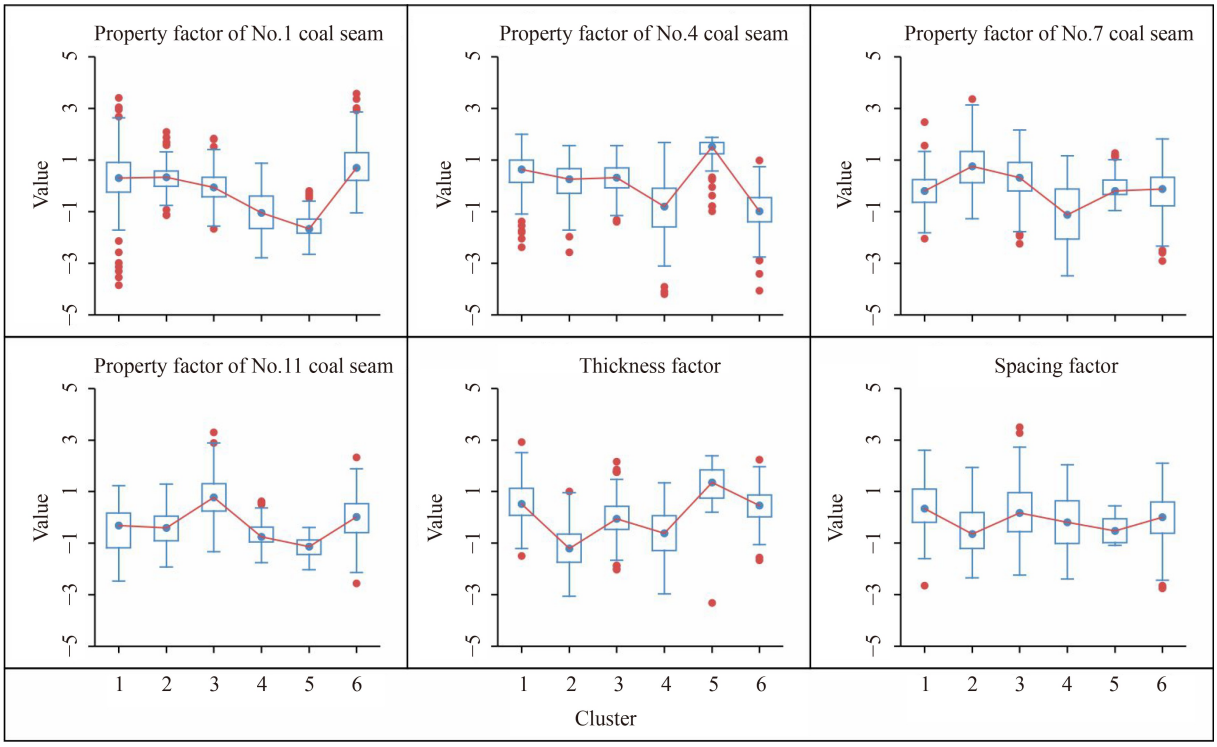

Fig. 15 Box plots of different clusters of factors.

Table 5 Model parameter characteristics of the 6 clusters

Clusters	Property	Thickness	Spacing between coal seams
1	—	All 4 coal seams are thicker	Spacing between Nos. 1 and 4 coal seams is smaller, the spacing between Nos. 4 and 7 coal seams is larger
2	The No. 7 coal seam has lower permeability and higher gas content	All 4 coal seams are thinner	Spacing between Nos. 1 and 4 coal seams is larger, the spacing between Nos. 4 and 7 coal seams is smaller
3	The No. 7 coal seam has higher gas content, the No. 11 coal seam has higher permeability and lower gas content	—	—
4	Nos. 1 and 7 coal seams have higher permeability and lower gas content, Nos. 4 and 11 coal seams have lower permeability and higher gas content	All 4 coal seams are thinner	Spacing between Nos. 1 and 4 coal seams and spacing between Nos. 4 and 7 coal seams are all smaller
5	Nos. 1 and 4 coal seams have higher permeability and lower gas content, Nos. 7 and 11 coal seams have lower permeability and gas content	Nos. 4 and 7 coal seams are thicker, Nos. 1 and 11 coal seams are relatively thinner	Spacing between Nos. 1 and 4 coal seams and spacing between Nos. 4 and 7 coal seams are all smaller
6	Nos. 1 and 4 coal seams have lower permeability and higher gas content, Nos. 7 and 11 coal seams have the higher gas content	—	—

Note: "—" or not mentioned indicates that the variable is at a medium level.

wells, the cavity completion in the horizontal section is accomplished by bottom hole pressure pulsing or alternating, allowing for a wider range of stress-relief could be realized than that of protective layer mining (Fig. 16(d)) (Sang et al., 2020). In addition, stress-relief CBM development through the horizontal well cavity completion is similar to open-hole cavity completion in vertical wells, which can eliminate reservoir damage caused by drilling fluid and coal fines (Vaziri and Palmer, 1998; Chen et al., 2014; Sang et al., 2020), and does not require the cooperation of adjacent layers. In the coal seam group, the stress state of the adjacent coal seam is bound to be affected after the cavity completion in the horizontal section, and it is also worth investigating whether it will cause a potential stress-relief zone similar to protective layer mining. The No. 11 coal seam in the study area is thicker with widely developed TDC, which is an ideal layer for stress-relief CBM development through the horizontal well cavity completion. The method is at the stage of theoretical research and preliminary engineering verification, and the related drilling, cavity completion, and gas-water drainage technology still need further improvement. The stress-relief CBM development through the horizontal well cavity completion was implemented in the No. 15 coal seam in the Zhengzhuang block in the southern Qinshui Basin, China,

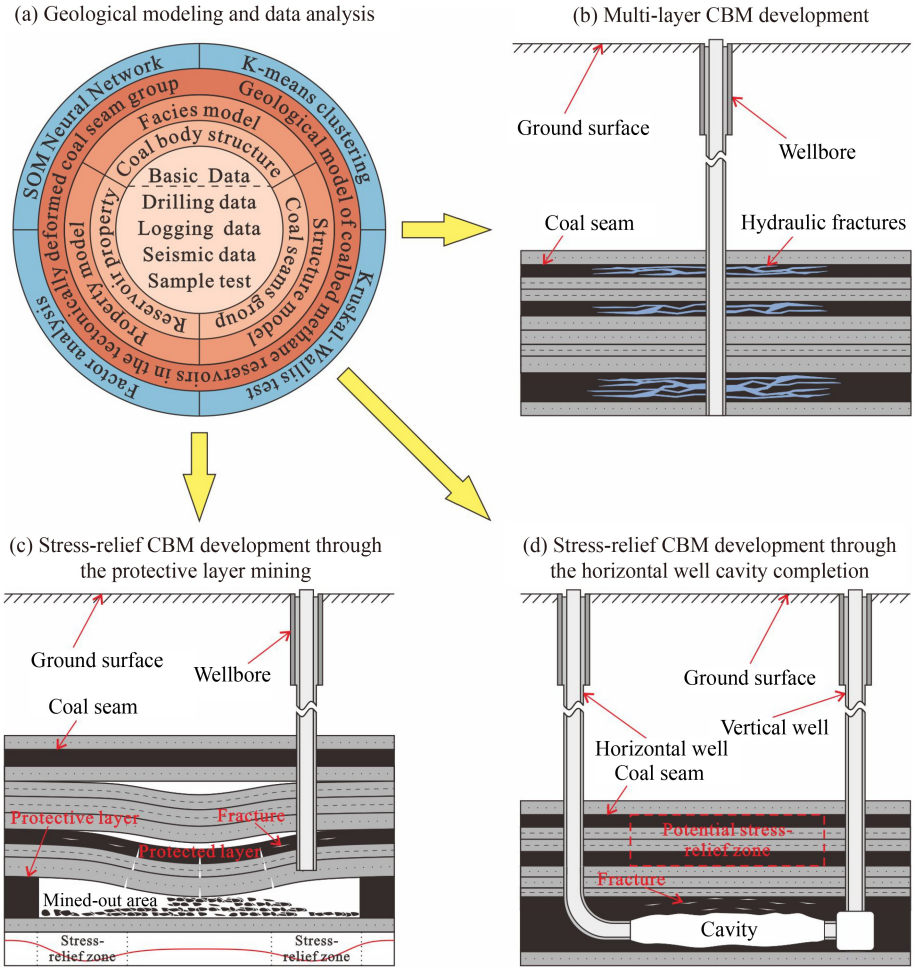

Fig. 16 Applications of geological modeling of CBM reservoirs in the TDC seam group.

showing excellent production enhancement, with stable daily gas production reaching 10000 m^3/d, which is 4 times the daily gas production of the adjacent hydraulically fractured horizontal well (Yang et al., 2022). Geological modeling of CBM reservoirs in the TDC seam group and its data analysis provide model parameters for numerical simulation for this method. In addition, more and more scholars prefer to use custom equations to numerically simulate the process and mechanism of CBM development, and the widely used equation-solving software includes COMSOL and ANSYS. The use of clustered model parameters is beneficial to simplify the model for numerical simulation and yield representative numerical simulation results. It can also improve the robustness of the numerical model and avoid the convergence difficulty of the numerical simulation due to the complex geometric model or the strong heterogeneity.

5 Conclusions

Taking the Dahebian block in western Guizhou as the study area, the geological model of coalbed methane reservoirs in the tectonically deformed coal seam group was established, and the spatial distribution pattern of model parameters was clarified by clustering algorithms and factor analysis. This study provides ideas for determining the permeability of TDC reservoirs, geological modeling of CBM reservoirs in the TDC seam group and its data analysis, which are significant for guiding the CBM development in the TDC seam group. The main conclusions are as follows.

1) The main coal body structures in Nos. 1, 4, and 7 coal seams are CC and GC; whereas the No. 11 coal seam is dominated by GC, which has larger thicknesses and spreads more continuously.

2) The *in situ* permeability of UC, CC, GC, and MC reservoirs are 0.333 mD, 0.931 mD, 0.146 mD, and 0.099 mD, respectively, according to the production performance analysis method. The gas content of CC is close to that of UC, while the TDC shows an obvious gas-bearing advantage.

3) The property model reveals that Nos. 1, 4, and 7 coal seams have a wider high-permeability area, but the gas content is lower; the TDC reservoirs are widely developed in the No. 11 coal seam, despite the higher gas

content, the overall permeability is low, and the high-permeability areas are discontinuously distributed, which is not conducive to CBM development.

4) The results of the SOM neural network and *K*-means clustering indicate that the geological model can be divided into 6 clusters, and the model parameter characteristics of the 6 clusters are summarized by data analysis in combination with the 6 factors extracted by factor analysis.

5) The cluster 3 with a lower thickness proportion of TDC reservoirs in the No. 11 coal seam is a more ideal choice for "hydraulic fracturing and multi-layer CBM development" in vertical wells. Nos. 1 and 7 coal seams of the cluster 4 with higher permeability and low risk of outburst are suitable as protective layers in stress-relief CBM development through the protective layer mining. The No. 11 coal seam is thicker with widely developed TDC, which is an ideal layer for stress-relief CBM development through the horizontal well cavity completion.

Acknowledgments This work was financially supported by the National Natural Science Foundation of China (Grant No. 41727801), the Geological Exploration Foundation of Guizhou Province (No. 208-9912-JBN-UTSO), and the Project Funded by the Priority Academic Program Development of Jiangsu Higher Education Institutions (PAPD).

References

Ahamed M A A, Perera M S A, Li D, Ranjith P G, Matthai S K (2019). Proppant damage mechanisms in coal seam reservoirs during the hydraulic fracturing process: a review. Fuel, 253: 615–629

Awotunde A A (2017). GLOCAL: a global-local optimization template for multiple history-matched reservoir parameters. J Petrol Sci Eng, 154: 1–18

Brentan B, Meirelles G, Luvizotto J E Jr, Izquierdo J (2018). Hybrid SOM+ k-Means clustering to improve planning, operation and management in water distribution systems. Environ Model Softw, 106: 77–88

Cao D, Wang A, Ning S, Li H, Guo A, Chen L, Liu K, Tan J, Zheng Z (2020). Coalfield structure and structural controls on coal in China. Int J Coal Sci Technol, 7(2): 220–239

Chen J, Peng R, Li S, Chen X (2017). Self-organizing feature map neural network and K-means algorithm as a data excavation tool for obtaining geological information from regional geochemical exploration data. Geophys Geochem Explor, 41: 919–927 (in Chinese)

Chen T, Wang Z, Yang G, Li J, Peng R (2014). Analysis of cavitation pressure difference during blowdown in CBM cavity completion. J Nat Gas Sci Eng, 18: 175–179

Cheng Y, Lei Y (2021). Causality between tectonic coal and coal and gas outbursts. J China Coal Soc, 46: 180–198 (in Chinese)

Cheng Y, Pan Z (2020). Reservoir properties of Chinese tectonic coal: a review. Fuel, 260: 116350

Choi B Y, Yun S T, Kim K H, Kim J W, Kim H M, Koh Y K (2014). Hydrogeochemical interpretation of South Korean groundwater monitoring data using self-organizing maps. J Geochem Explor, 137: 73–84

Davies D L, Bouldin D W (1979). A cluster separation measure. IEEE Trans Pattern Anal Mach Intell, PAMI-1(2): 224–227

Dong J, Cheng Y, Hu B, Hao C, Tu Q, Liu Z (2018). Experimental study of the mechanical properties of intact and tectonic coal via compression of a single particle. Powder Technol, 325: 412–419

Dunlop E C, Salmachi A, McCabe P J (2020). Investigation of increasing hydraulic fracture conductivity within producing ultra-deep coal seams using time-lapse rate transient analysis: a long-term pilot experiment in the Cooper Basin, Australia. Int J Coal Geol, 220: 103363

Fu X, Qin Y, Wang G, Rudolph V (2009). Evaluation of coal structure and permeability with the aid of geophysical logging technology. Fuel, 88(11): 2278–2285

GB/T 30050-2013 (2013). Classification of Coal Structure. National Standards of the People's Republic of China (in Chinese)

Guo C, Qin Y, Wu C, Lu L (2020). Hydrogeological control and productivity modes of coalbed methane commingled production in multi-seam areas: a case study of the Bide–Santang Basin, western Guizhou, south China. J Petrol Sci Eng, 189: 107039

Guo D, Han D, Zhang J (2002). Research on the occurrence and distribution of structural coal in Pingdingshan coal district. J China Coal Soc, 27: 249–253 (in Chinese)

Hamdi H (2014). Well-test response in stochastic permeable media. J Petrol Sci Eng, 119: 169–184

Huang H, Sang S, Fang L, Li G, Xu H, Ren B (2010). Optimum location of surface wells for remote pressure relief coalbed methane drainage in mining areas. Mining Sci Techn (China), 20(2): 230–237

Jiang W, Zhang P, Li D, Li Z, Wang J, Duan Y, Wu J, Liu N (2022). Reservoir characteristics and gas production potential of deep coalbed methane: insights from the No. 15 coal seam in shouyang block, Qinshui Basin, China. Unconventional Resour, 2: 12–20

Ju Y, Wang G, Hu C (2002). Tectonic deformation and its control over thickness of coal seams in Haizi Coal Mine. J China Univ Min Technol, 31: 374–379 (in Chinese)

Kalteh A M, Hjorth P, Berndtsson R (2008). Review of the self-organizing map (SOM) approach in water resources: analysis, modelling and application. Environ Model Softw, 23(7): 835–845

Karacan C Ö (2013). Production history matching to determine reservoir properties of important coal groups in the Upper Pottsville formation, Brookwood and Oak Grove fields, Black Warrior Basin, Alabama. J Nat Gas Sci Eng, 10: 51–67

Kohonen T (1982). Self-organized formation of topologically correct feature maps. Biol Cybern, 43(1): 59–69

Kohonen T (1995). Self-Organizing Maps. New York: Springer

Lang Z (2001). Mechanics of oil and gas flow in porous media. Dongying: Petroleum University Press

Langmuir I (1918). The adsorption of gases on plane surfaces of glass, mica and platinum. J Am Chem Soc, 40(9): 1361–1403

Li C, Peng C, Zhu S (2013). Coalbed methane is adsorption gas

underground. Lithologic Reservoirs, 25: 112–115+122 (in Chinese)

Li F, Jiang B, Cheng G, Song Y, Tang Z (2019). Structural and evolutionary characteristics of pores-microfractures and their influence on coalbed methane exploitation in high-rank brittle tectonically deformed coals of the Yangquan mining area, northeastern Qinshui Basin, China. J Petrol Sci Eng, 174: 1290–1302

Li M, Wen Q, Zhang Y, Chen Z (2022c). New insights into the transformation of effluent organic matter during Fe(II)-assisted advanced oxidation processes: parallel factor analysis coupled with self-organizing maps. Water Res, 221: 118789

Li S, Tang D, Pan Z, Xu H, Guo L (2015). Evaluation of coalbed methane potential of different reservoirs in western Guizhou and eastern Yunnan, China. Fuel, 139: 257–267

Li W, Jiang B, Moore T A, Wang G, Liu J G, Song Y (2017a). Characterization of the chemical structure of tectonically deformed coals. Energy Fuels, 31(7): 6977–6985

Li Y, Pan S, Ning S, Shao L, Jing Z, Wang Z (2022a). Coal measure metallogeny: metallogenic system and implication for resource and environment. Sci China Earth Sci, 65(7): 1211–1228

Li Y, Wang Z, Tang S, Elsworth D (2022b). Re-evaluating adsorbed and free methane content in coal and its ad-and desorption processes analysis. Chem Eng J, 428: 131946

Li Y, Zhang C, Tang D, Gan Q, Niu X, Wang K, Shen R (2017b). Coal pore size distributions controlled by the coalification process: an experimental study of coals from the Junggar, Ordos and Qinshui basins in China. Fuel, 206: 352–363

Liu J, Chang S, Zhang S, Li Y, Chen Q (2022). Integrated seismic–geological prediction of tectonic coal via main controlling factors. Acta Geophys, 70(1): 173–190

Liu J, Jiang B, Li M, Qu Z, Wang L, Li L (2015). Structural control on pore-fracture characteristics of coals from Xinjing coal mine, northeastern Qinshui Basin, China. Arab J Geosci, 8(7): 4421–4431

MacQueen J (1967). Some methods for classification and analysis of multivariate observations. Proceedings of the Fifth Berkeley Symposium on Mathematical Statistics and Probability, 1: Statistics: 281–297

Mukherjee A (1997). Self-organizing neural network for identification of natural modes. J Comput Civ Eng, 11(1): 74–77

Pan J, Niu Q, Wang K, Shi X, Li M (2016). The closed pores of tectonically deformed coal studied by small-angle X-ray scattering and liquid nitrogen adsorption. Microporous Mesoporous Mater, 224: 245–252

Qin Y, Gao D (2012). Prediction of Evaluation of Coalbed Methane Resources Potential in Guizhou Province. Xuzhou: China University of Mining and Technology Press (in Chinese)

Qin Y, Moore T A, Shen J, Yang Z, Shen Y, Wang G (2018). Resources and geology of coalbed methane in China: a review. Int Geol Rev, 60(5–6): 777–812

Salmachi A, Dunlop E, Rajabi M, Yarmohammadtooski Z, Begg S (2019). Investigation of permeability change in ultradeep coal seams using time-lapse pressure transient analysis: a pilot project in the Cooper Basin, Australia. AAPG Bull, 103(1): 91–107

Salmachi A, Haghighi M (2012). Temperature effect on methane sorption and diffusion in coal: application for thermal recovery from coal seam gas reservoirs. APPEA J, 52(1): 291–300

Salmachi A, Rajabi M, Wainman C, Mackie S, McCabe P, Camac B, Clarkson C (2021). History, geology, *in situ* stress pattern, gas content and permeability of coal seam gas basins in Australia: a review. Energies, 14(9): 2651

Sang S, Xu H, Fang L, Li G, Huang H (2010). Stress relief coalbed methane drainage by surface vertical wells in China. Int J Coal Geol, 82(3–4): 196–203

Sang S, Zhou Z, Liu S, Wang H, Cao L, Liu H, Li Z, Zhu S, Liu C, Huang H, Xu H, Wang R, Jiang J, Ashutosh T, Han S (2020). Research advances in theory and technology of the stress release applied extraction of coalbed methane from tectonically deformed coals. J China Coal Soc, 45: 2531–2543 (in Chinese)

Santos M R, Roisenberg A, Iwashita F, Roisenberg M (2020). Hydrogeochemical spatialization and controls of the Serra Geral Aquifer System in southern Brazil: a regional approach by self-organizing maps and k-means clustering. J Hydrol (Amst), 591: 125602

Shen Y, Qin Y, Guo Y, Ren H, Wei Z, Xie G (2012). The Upper Permian coalbed methane bearing system and its sedimentary control in western Guizhou, China. Geol J Chin Univ, 18: 427–432 (in Chinese)

Shi J, Wang S, Wang K, Liu C, Wu S, Sepehrnoori K (2019). An accurate method for permeability evaluation of undersaturated coalbed methane reservoirs using early dewatering data. Int J Coal Geol, 202: 147–160

Shi J, Wang S, Zhang H, Sun Z, Hou C, Chang Y, Xu Z (2018). A novel method for formation evaluation of undersaturated coalbed methane reservoirs using dewatering data. Fuel, 229: 44–52

Shi J, Wu J, Sun Z, Xiao Z, Liu C, Sepehrnoori K (2020). Methods for simultaneously evaluating reserve and permeability of undersaturated coalbed methane reservoirs using production data during the dewatering stage. Petrol Sci, 17(4): 1067–1086

Sibbit A M, Faivre O (1985). The dual laterolog response in fractured rocks. SPWLA 26th Annual Logging Symposium, Dallas: Texas

Skoczylas N, Dutka B, Sobczyk J (2014). Mechanical and gaseous properties of coal briquettes in terms of outburst risk. Fuel, 134: 45–52

Song C, Zhi S, Feng G, Lin J (2021). Enhancing potential of hydrofracturing in mylonitic coal by biocementation. Energy Sci Eng, 9(4): 565–576

Syakur M A, Khotimah B K, Rochman E M S, Satoto B D (2018). Integration k-means clustering method and elbow method for identification of the best customer profile cluster. IOP Conf Series Mater Sci Eng, 336: 012017

Tao S, Chen S, Pan Z (2019). Current status, challenges, and policy suggestions for coalbed methane industry development in China: a review. Energy Sci Eng, 7(4): 1059–1074

Urych T, Głogowska M, Warzecha R, Wątor A, Chećko J (2019). 3D model of hard coal deposit and analysis of the possibility of using it to plan deposit management. Int Multidiscip Sci Geoconf SGEM, 19: 3–13

Vaziri H H, Palmer I D (1998). Evaluation of openhole cavity completion technique in coalbed methane reservoirs. Int J Rock Mech Min Sci, 35(4–5): 523–524

Vesanto J, Himberg J, Alhoniemi E, Parhankagas J (2000). SOM Toolbox for Matlab 5, Report A57

Wang H, Shao L, Hao L, Zhang P, Glasspool I J, Wheeley J R, Wignall P B, Yi T, Zhang M, Hilton J (2011). Sedimentology and sequence stratigraphy of the Lopingian (Late Permian) coal measures in southwestern China. Int J Coal Geol, 85(1): 168–183

Wang L, Lu Z, Chen D, Liu Q, Chu P, Shu L, Ullah B, Wen Z (2020). Safe strategy for coal and gas outburst prevention in deep-and-thick coal seams using a soft rock protective layer mining. Saf Sci, 129: 104800

Wang Y, Liu D, Cai Y, Yao Y, Zhou Y (2018). Evaluation of structured coal evolution and distribution by geophysical logging methods in the Gujiao Block, northwest Qinshui Basin, China. J Nat Gas Sci Eng, 51: 210–222

Xu H, Sang S, Fang L, Huang H, Ren B (2011). Failure characteristics of surface vertical wells for relieved coal gas and their influencing factors in Huainan mining area. Mining Sci Tech (China), 21(1): 83–88

Xu H, Sang S, Yang J, Chen J (2016). Status and expectation on coalbed methane exploration and development in Guizhou Province. Coal Sci Techn, 44: 1–7+196 (in Chinese)

Yang R, Huang Z, Li G, Chen J, Wen H, Qin X (2022). Feasibility investigation of hydraulic jet multistage cavity completion in coalbed methane horizontal wells. J China Coal Soc, 47: 3284–3297 (in Chinese)

Yang W, Lin B, Qu Y, Li Z, Zhai C, Jia L, Zhao W (2011). Stress evolution with time and space during mining of a coal seam. Int J Rock Mech Min Sci, 48(7): 1145–1152

Yang Z, Zhang Z, Qin Y, Wu C, Yi T, Li Y, Tang J, Chen J (2018). Optimization methods of production layer combination for coalbed methane development in multi-coal seams. Pet Explor Dev, 45(2): 312–320

Yuan L (2015). Theory and practice of integrated coal production and gas extraction. Int J Coal Sci Technol, 2(1): 3–11

Zhang X, Du Z, Li P (2017). Physical characteristics of high-rank coal reservoirs in different coal-body structures and the mechanism of coalbed methane production. Sci China Earth Sci, 60(2): 246–255

Zhao Y, Shi Z, Hao S, Liu J, Yang Z, Wang S (2014). Well completion technology using screen pipe for horizontally-intersected well in soft coal seam. Procedia Eng, 73: 311–317

Zhou F, Allinson G, Wang J, Sun Q, Xiong D, Cinar Y (2012). Stochastic modelling of coalbed methane resources: a case study in Southeast Qinshui Basin, China. Int J Coal Geol, 99: 16–26

Zhou F, Guan Z (2016). Uncertainty in estimation of coalbed methane resources by geological modelling. J Nat Gas Sci Eng, 33: 988–1001

Zhu S, Salmachi A, Du Z (2018). Two phase rate-transient analysis of a hydraulically fractured coal seam gas well: a case study from the Ordos Basin, China. Int J Coal Geol, 195: 47–60